Supplement of Atmos. Chem. Phys., 25, 10109–10139, 2025
https://doi.org/10.5194/acp-25-10109-2025-supplement

Atmospheric Chemistry and Physics
Open Access
EGU

Supplement of

Covariability of dynamics and composition in the Asian monsoon tropopause layer from satellite observations and reanalysis products

Shenglong Zhang et al.

Correspondence to: Jonathon S. Wright (jswright@tsinghua.edu.cn)

Summary

This online supplement contains 27 figures that support the reanalysis intercomparison component of this paper by extending evaluations presented in the main text to additional reanalysis products:

(1) **Figures S1–S3.** Total diabatic heating anomalies from ERA5, MERRA-2, and JRA-3Q regressed onto the first three principal components from Aura MLS (Figure 4 in the main text).

(2) **Figures S4–S7.** Partial column water vapor anomalies from Aura MLS, M2-SCREAM, ERA5, CAMS, and JRA-3Q regressed onto the principal components above the tropopause and below the tropopasue from Aura MLS (Figure 7 in the main text).

(3) **Figures S8–S9.** Dynamical and physical budget anomalies from ERA5, MERRA-2, and JRA-3Q regressed onto the first principal component (PC1) trend variability above the tropopause ($\mathrm{PC1}^{\mathrm{strat}}_{\mathrm{TREND}}$) from Aura MLS.

(4) **Figure S10–S12.** Yearly variations in model internal dynamics, physics, and assimilation effects over the northwestern and northeastern quadrants and budget analysis above and below the tropopause over the southwestern and southeastern quadrants (Figure 8 in the main text).

(5) **Figures S13–S15.** Water vapor, ozone, and dynamical and thermodynamic anomalies regressed onto the interannual variability of first principal component from Aura MLS for all reanalysis products (Figure 10 in the main text).

(4) **Figure S16.** CO anomalies regressed onto the first three principal components from Aura MLS (Figures 10d, 13d, and 14d in the main text).

(6) **Figure S17.** Direct lead–lag comparisons supporting the quadratic cycle of water vapor among the moist and dry phase of the second and third principal components (Figure 12 in the main text).

(7) **Figures S18–S24.** Water vapor, ozone, and dynamical and thermodynamic anomalies regressed onto the second and third principal components from Aura MLS for all reanalysis products (Figures 12–15 in the main text).

(8) **Figures S25–S27.** Anomalous water vapor tendencies for ERA5, JRA-3Q, and MERRA-2 composited for the moist and dry phases of the second and third principal components based on Aura MLS (Figure 16 in the main text).

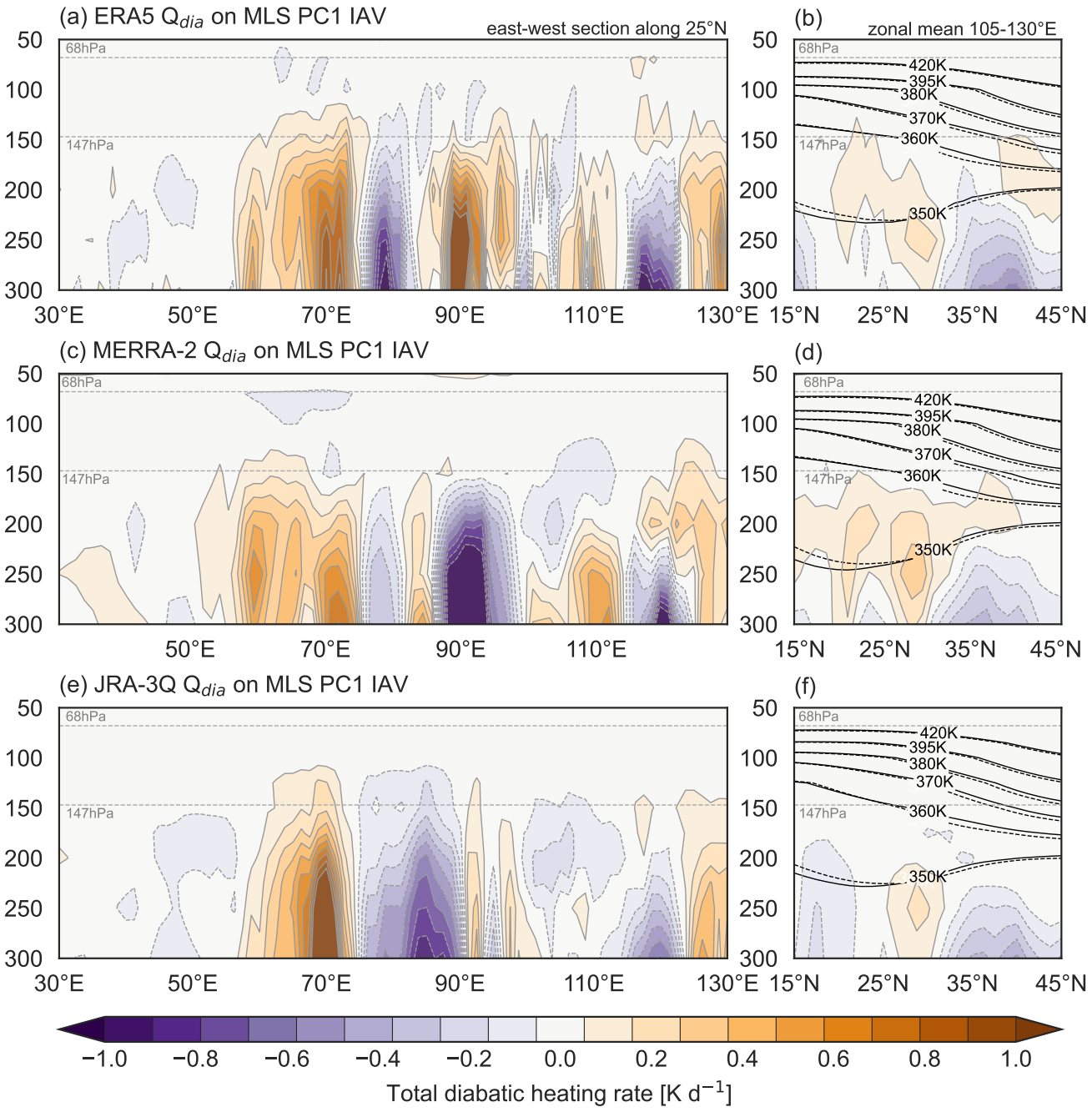

Figure S1. Composite diabatic heating anomalies based on (a)–(b) ERA5, (c)–(d) MERRA-2, (e)–(f) JRA-3Q conditioned on the interannual variability component of PC1 of LSWV variability from Aura MLS (Fig. 1c, Fig. 3c). Composite anomalies are calculated as the difference between averages over pentads with $\mathrm{PC1} \geq 1$ and pentads with $\mathrm{PC1} \leq -1$. Diabatic heating anomalies are evaluated (a,c,e) along 25°N and (b,d,f) zonally averaged over 105°E–130°E. Zonal mean isentropic surfaces (black contours in right column) are shown for both $\mathrm{PC1} \geq 1$ (solid lines) and $\mathrm{PC1} \leq -1$ (dotted lines). This figure shows results based on multiple reanalyses as context for Figure 4a in the main text.

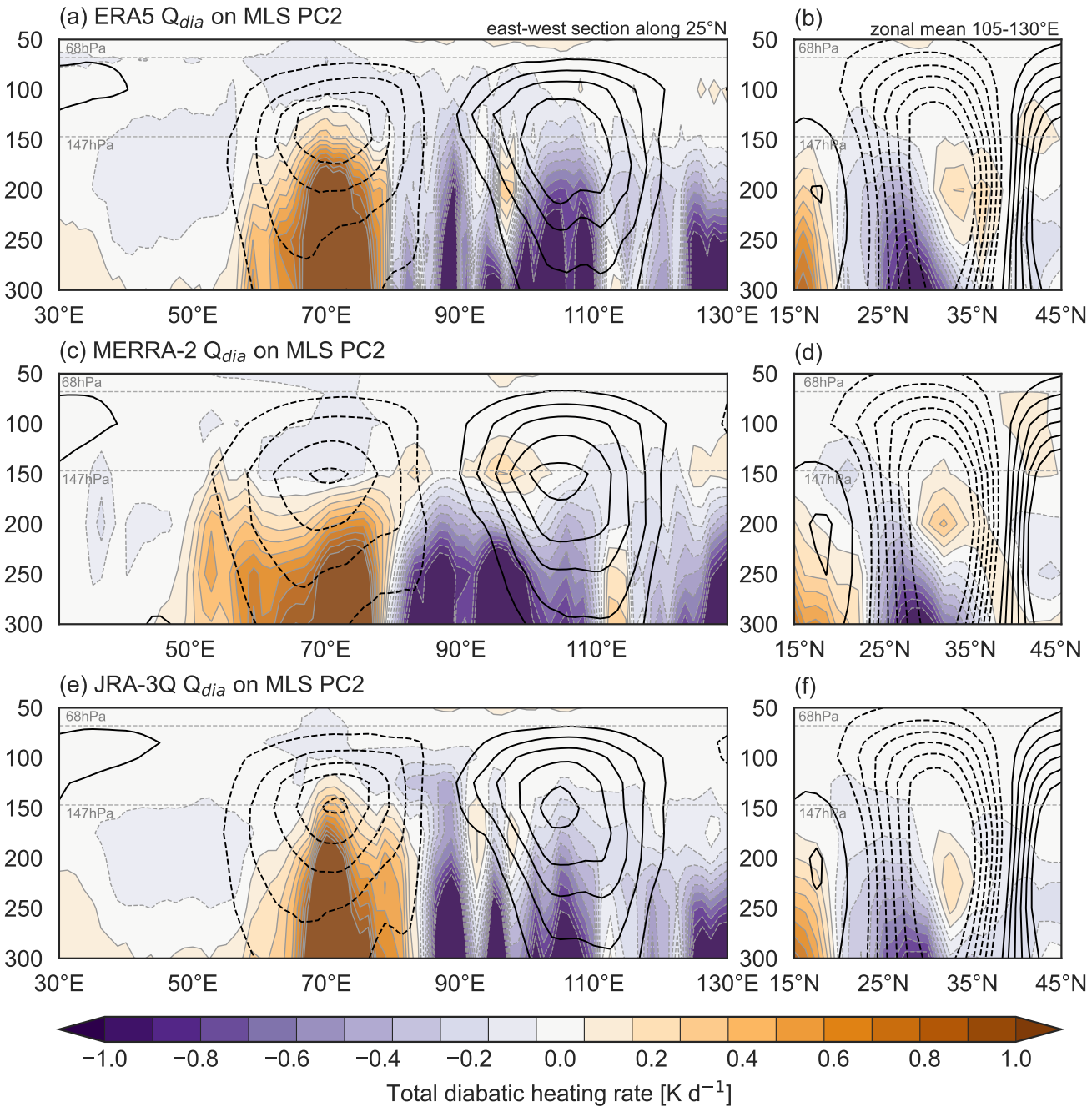

Figure S2. Composite diabatic heating anomalies based on (a)–(b) ERA5, (c)–(d) MERRA-2, (e)–(f) JRA-3Q conditioned on the second principal component (PC2) of LSWV variability from Aura MLS (Fig. 2a, Fig. 3d). Composite anomalies are calculated as the difference between averages over pentads with PC2 ≥ 1 and pentads with PC2 ≤ -1. Diabatic heating anomalies are evaluated (a,c,e) along 25°N and (b,d,f) zonally averaged over 105°E–130°E. Meridional (a,c,e) and zonal (b,d,f) wind anomalies (black contours) are shown at intervals of 1 m s^{-1} from ± 1 m s^{-1}. This figure shows results based on multiple reanalyses as context for Figure 4b in the main text.

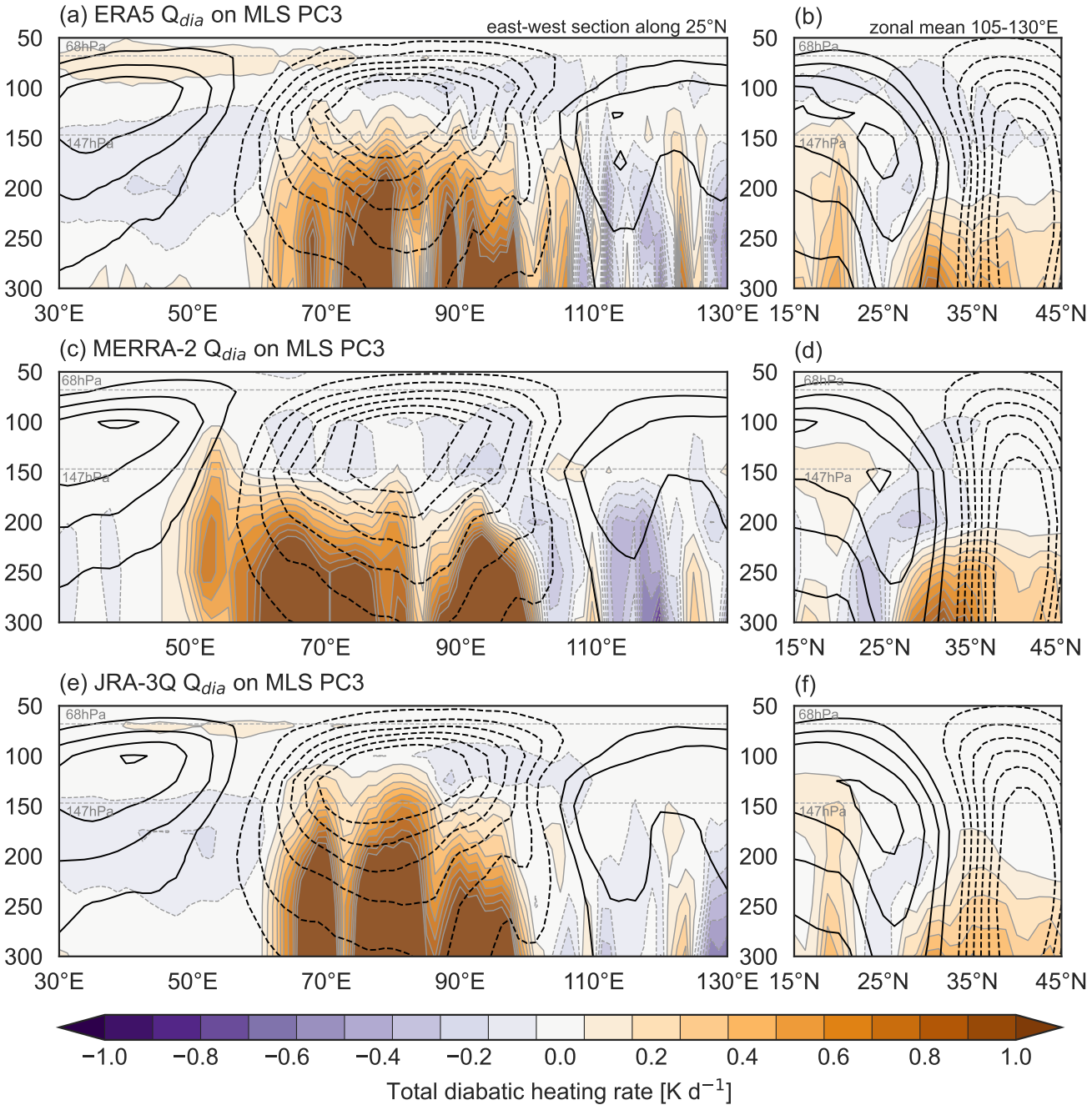

Figure S3. Composite diabatic heating anomalies based on (a)–(b) ERA5, (c)–(d) MERRA-2, (e)–(f) JRA-3Q conditioned on the third principal component (PC3) of LSWV variability from Aura MLS (Fig. 2b, Fig. 3e). Composite anomalies are calculated as the difference between averages over pentads with $\mathrm{PC3} \geq 1$ and pentads with $\mathrm{PC3} \leq -1$. Diabatic heating anomalies are evaluated (a,c,e) along 25°N and (b,d,f) zonally averaged over 105°E–130°E. Meridional (a,c,e) and zonal (b,d,f) wind anomalies (black contours) are shown at intervals of $1\,\mathrm{m\,s^{-1}}$ from $\pm 1\,\mathrm{m\,s^{-1}}$. This figure shows results based on multiple reanalyses as context for Figure 4c in the main text.

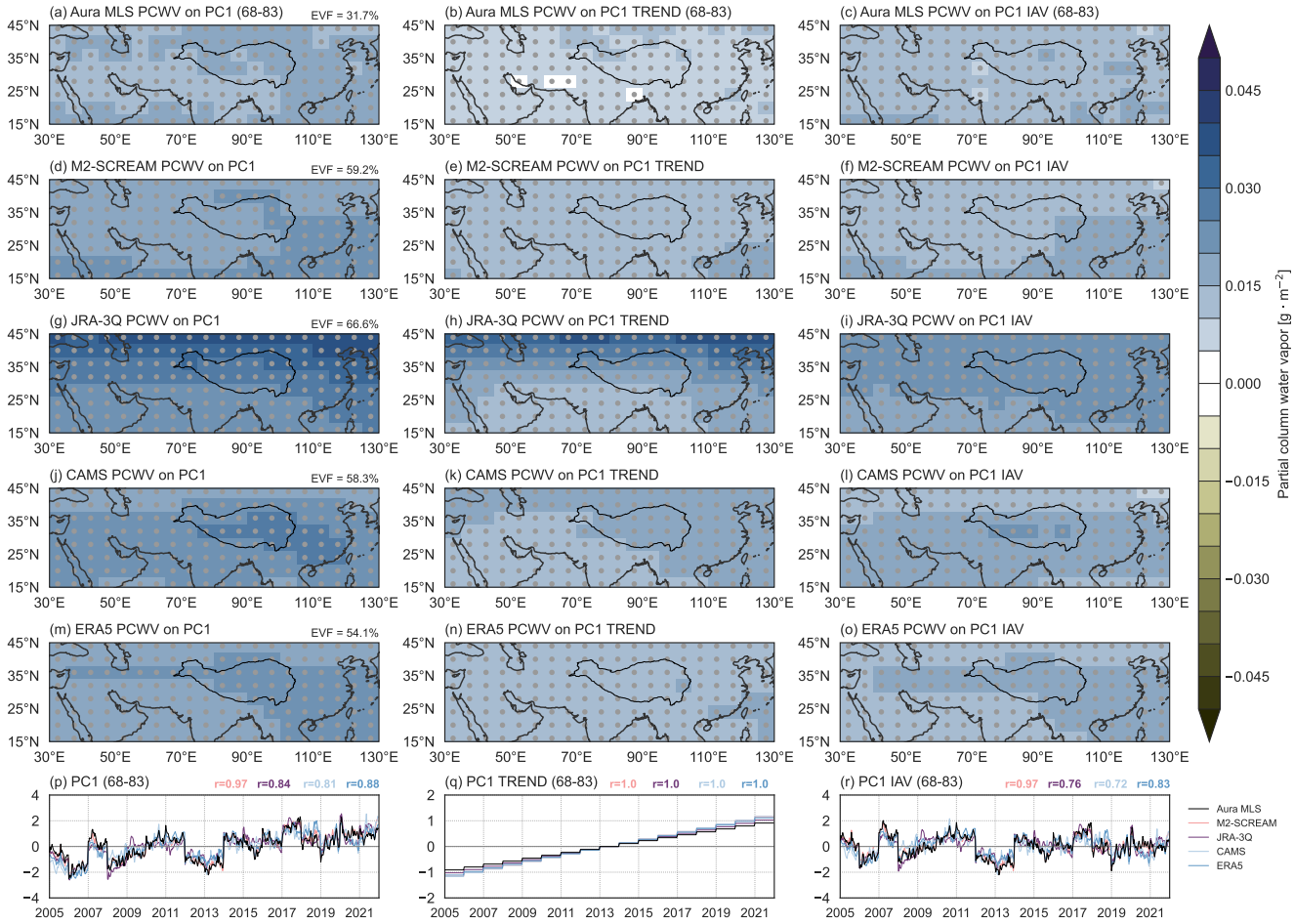

Figure S4. Deseasonalized partial-column water vapor (PCWV) anomalies integrated from 83 to 68 hPa regressed onto the (a) first principal component (PC1) from Aura MLS and its (b) trend ($PC1_{TREND}$) and (c) interannual variability ($PC1_{IAV}$) components; (d)–(f) same as (a)–(c), but for PC1 from M2-SCREAM; (g)–(i) same as (a)–(c), but for PC1 from JRA-3Q; (j)–(l) same as (a)–(c), but for PC1 from CAMS; (m)–(o) same as (a)–(c), but for PC1 from ERA5; and (p)–(r) the corresponding principal component time series. Principal components (PCs) are based on EOF analysis of vertical and horizontal variations in water vapor for the two Aura MLS pressure levels within 68 hPa–83 hPa, 30°E–130°E, and 15°N–45°N. Red contours mark the location of the Tibetan Plateau, with stippling indicating significance at the 95% confidence level based on Student's t test. The fraction of total variance explained by each mode is listed at the upper right of panels(a,d,g,j,m). Correlations between MLS-based PCs and those based on M2-SCREAM (light red), JRA-3Q (purple), CAMS (light blue), and ERA5 (dark blue) are listed from right to left along the tops of panels (p)–(r).

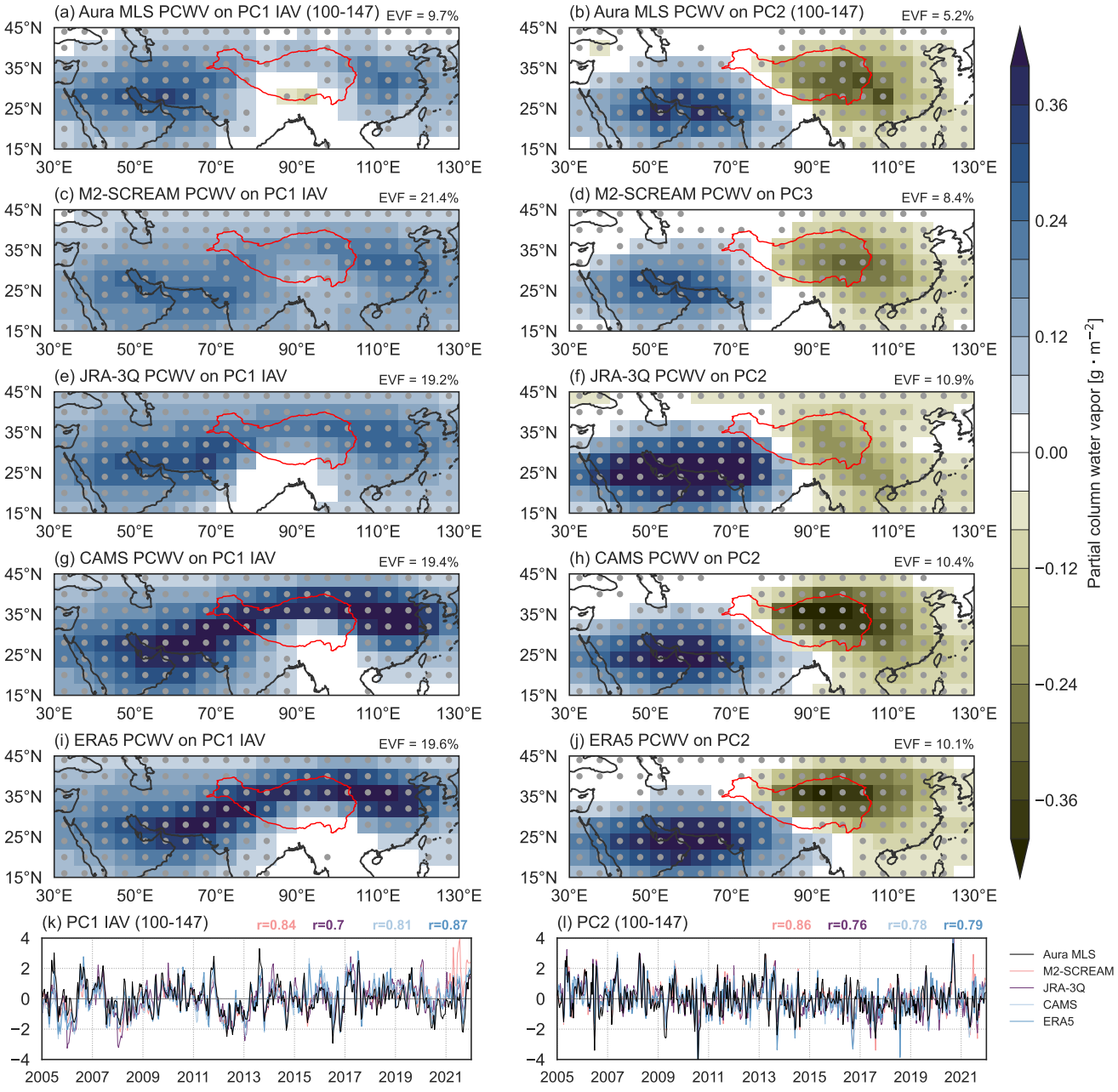

Figure S5. Deseasonalized partial-column water vapor (PCWV) anomalies integrated from 147 to 100 hPa regressed onto the (a) first principal component (PC1) interannual variability ($PC1_{IAV}$) and (b) the second principal component (PC2) from Aura MLS; (c)–(d) same as (a)–(b), but for $PC1_{IAV}$ and PC2 from M2-SCREAM; (e)–(f) same as (a)–(b), but for $PC1_{IAV}$ and PC2 from JRA-3Q; (g)–(h) same as (a)–(b), but for $PC1_{IAV}$ and PC2 from CAMS; (i)–(j) same as (a)–(b), but for $PC1_{IAV}$ and PC2 from ERA5; and (k)–(l) the corresponding principal component time series. Principal components (PCs) are based on EOF analysis of vertical and horizontal variations in water vapor for the three Aura MLS pressure levels within 100 hPa–147 hPa, 30°E–130°E, and 15°N–45°N. Red contours mark the location of the Tibetan Plateau, with stippling indicating significance at the 95% confidence level based on Student's t test. The fraction of total variance explained by each mode is listed at the upper right of panels(a–j). Correlations between MLS-based PCs and those based on M2-SCREAM (light red), JRA-3Q (purple), CAMS (light blue), and ERA5 (dark blue) are listed from right to left along the tops of panels (k)–(l).

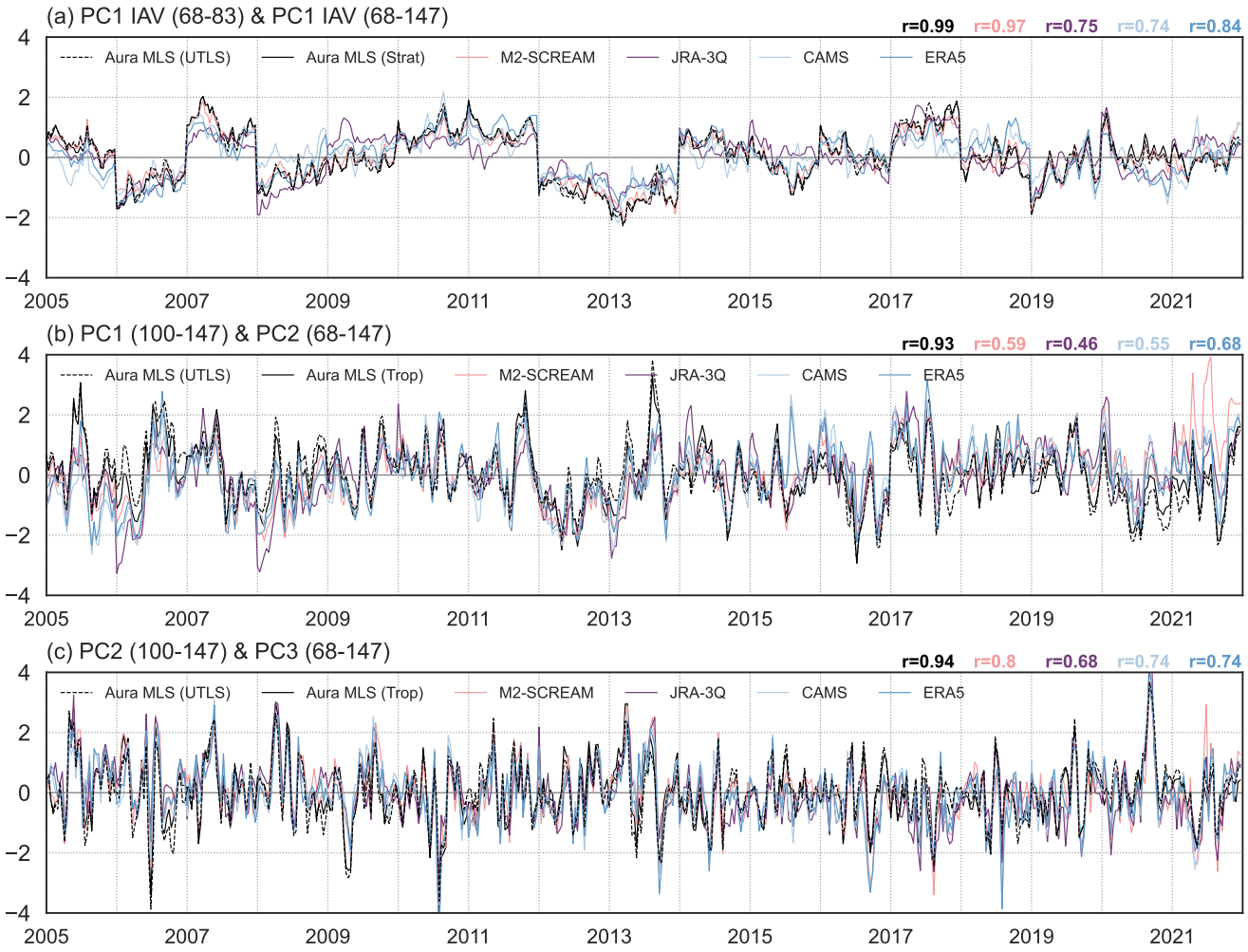

Figure S6. Principal component (PC) time series for the spatial patterns shown in Figs. S4 and S5 based on Aura MLS (black), ERA5 (dark blue), CAMS (light blue), JRA-3Q (purple), and M2-SCREAM (light red) and PCs shown in the manuscript based on Aura MLS (dashed black). Time series are shown for (a) the first principal component (PC1) interannual variability in the UTLS ($PC1_{IAV}$) and above the tropopause ($PC1_{IAV}^{strat}$); (b) the second principal component (PC2) in the UTLS and PC1 interannual variability below the tropopause ($PC1_{IAV}^{trop}$); and (c) the third principal component (PC3) in the UTLS and PC2 below the tropopause ($PC2^{trop}$). PCs in the UTLS are based on EOF analysis of vertical and horizontal variations in water vapor for the five Aura MLS pressure levels within 68 hPa–147 hPa, 30°E–130°E, and 15°N–45°N; PCs above the tropopause are based on EOF analysis of vertical and horizontal variations in water vapor for the three Aura MLS pressure levels within 68 hPa–83 hPa, 30°E–130°E, and 15°N–45°N; and PCs below the tropopause are based on EOF analysis of vertical and horizontal variations in water vapor for the three Aura MLS pressure levels within 100 hPa–147 hPa, 30°E–130°E, and 15°N–45°N. Correlations between MLS-based PCs in the UTLS and those based on MLS above/below the tropopause (black), M2-SCREAM (light red), JRA-3Q (purple), CAMS (light blue), and ERA5 (dark blue) are listed from right to left along the tops of panels (a–c).

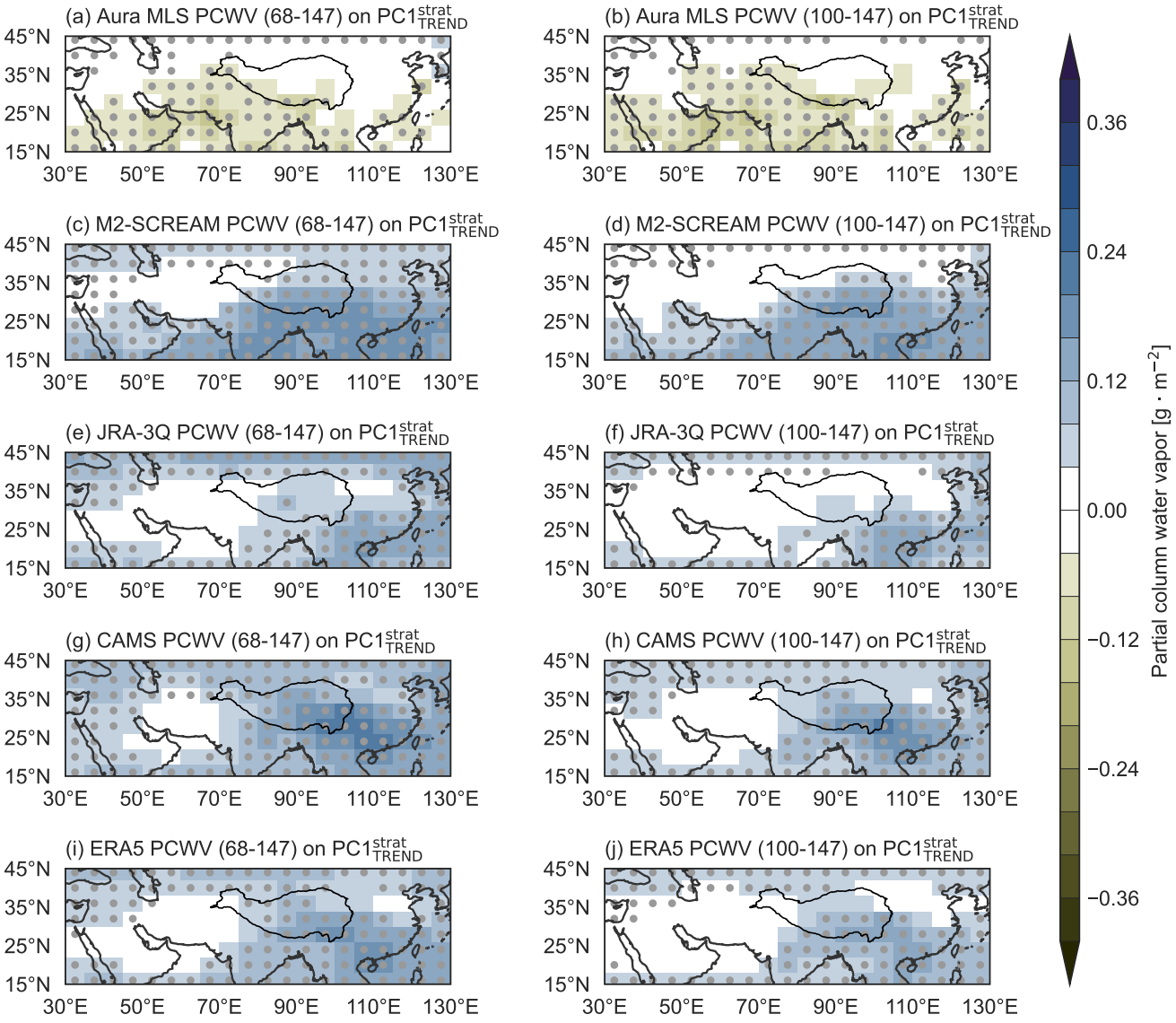

Figure S7. Deseasonalized partial-column water vapor (PCWV) anomalies integrated (a) from 147 to 68 hPa and (b) from 147 to 100 hPa regressed onto the first principal component (PC1) trend variability ($PC1_{TREND}$) from Aura MLS (Fig. S4q); (c)–(d) same as (a)–(b), but for PCWV from M2-SCREAM; (e)–(f) same as (a)–(b), but for PCWV from JRA-3Q; (g)–(h) same as (a)–(b), but for PCWV from CAMS; (i)–(j) same as (a)–(b), but for PCWV from ERA5. Principal components (PCs) are based on EOF analysis of vertical and horizontal variations in water vapor for the two Aura MLS pressure levels within 68 hPa–83 hPa, 30°E–130°E, and 15°N–45°N. Red contours mark the location of the Tibetan Plateau, with stippling indicating significance at the 95% confidence level based on Student's t test.

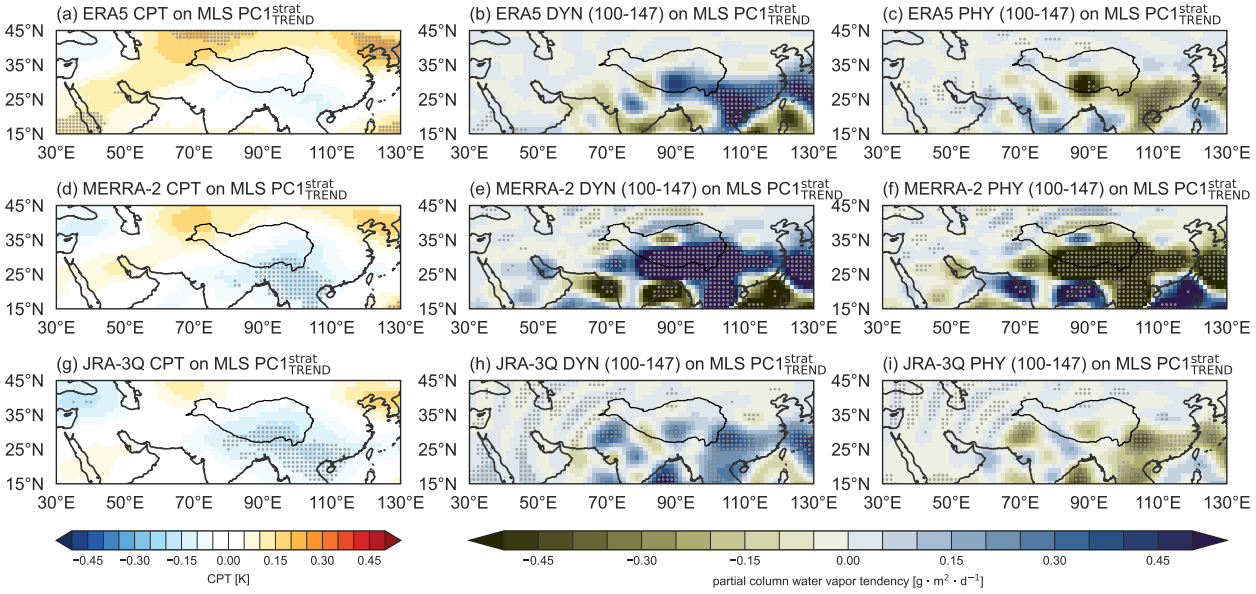

Figure S8. (a) Changes in cold point tropopause (CPT) temperatures, (b) dynamics term, and (c) physics term based on ERA5 regressed onto the first principal component (PC1) trend variability above the tropopause ($PC1^{strat}_{TREND}$) from Aura MLS. (d–f) same as (a–c), but for MERRA-2. (g–i) same as (a–c), but for JRA-3Q. Dynamics and physcial terms are integrated from 147 to 100 hPa. The location of the Tibetan Plateau is marked by a black contour in all panels. Stippling indicates locations where regression slopes are significant at the 95% confidence level based on Student's t test.

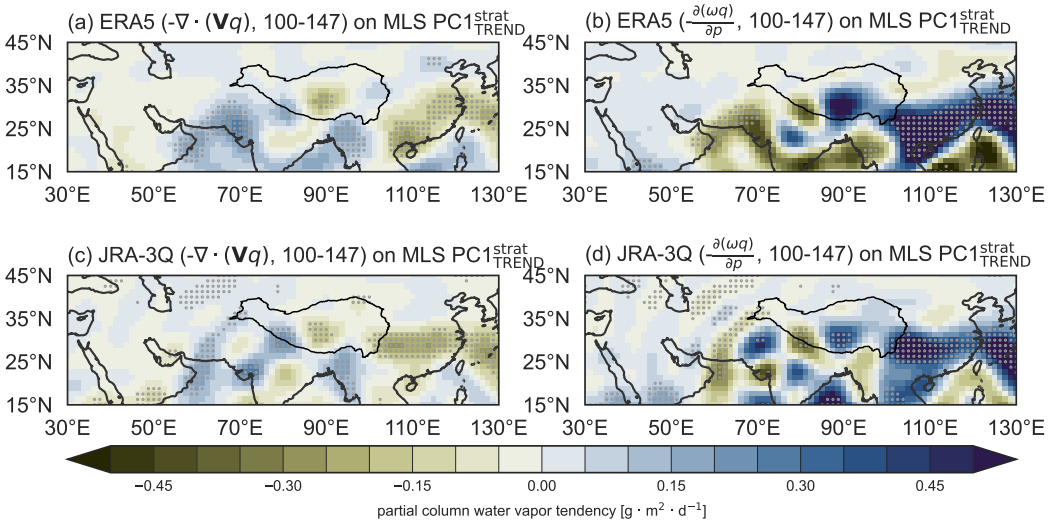

Figure S9. Changes in (a) horizontal moisture flux convergence ($-\nabla \cdot (\mathbf{V}q)$), (b) vertical moisture flux convergence ($-\frac{\partial(\omega q)}{\partial p}$) based on ERA5 regressed onto the first principal component (PC1) trend variability above the tropopause ($PC1^{strat}_{TREND}$) from Aura MLS. (c–d) same as (a–b), but for JRA-3Q. Horizontal and vertical moisture flux convergence terms are integrated from 147 to 100 hPa. The location of the Tibetan Plateau is marked by a black contour in all panels. Stippling indicates locations where regression slopes are significant at the 95% confidence level based on Student's t test.

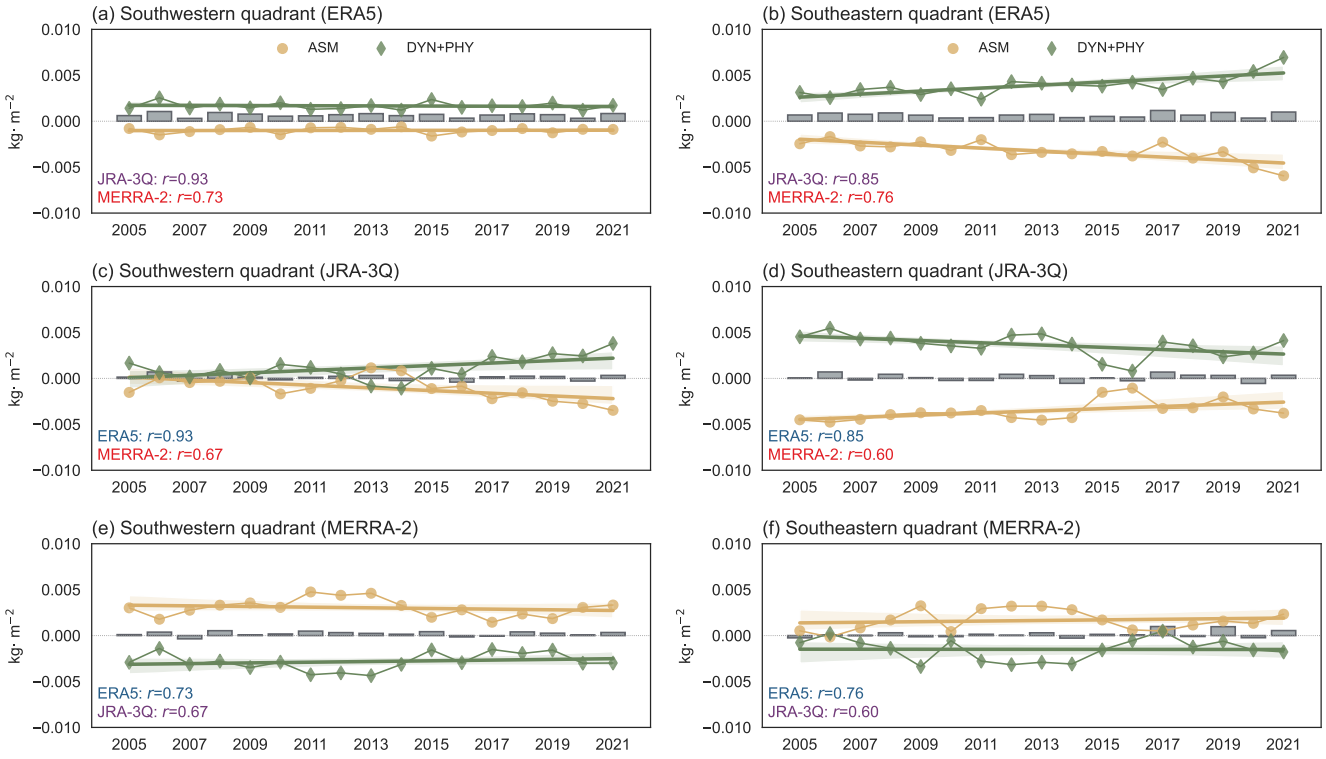

Figure S10. Yearly variations in the sum of the dynamics and physics terms (green lines), assimilation increments (yellow lines), and time rate of changes in partial column water vapor (gray boxes) in the monsoon tropopause layer based on (a,b) ERA5, (c,d) JRA-3Q, and (e,f) MERRA-2 over (a,c,e) the northwestern quadrant (25°N–45°N,30°E–90°E) and (b,d,f) the northeastern quadrant (25°N–45°N,90°E–130°E) of the monsoon anticyclone. Correlation coefficients between net water vapor tendency time series based on individual reanalyses are listed in the lower left corner of each panel.

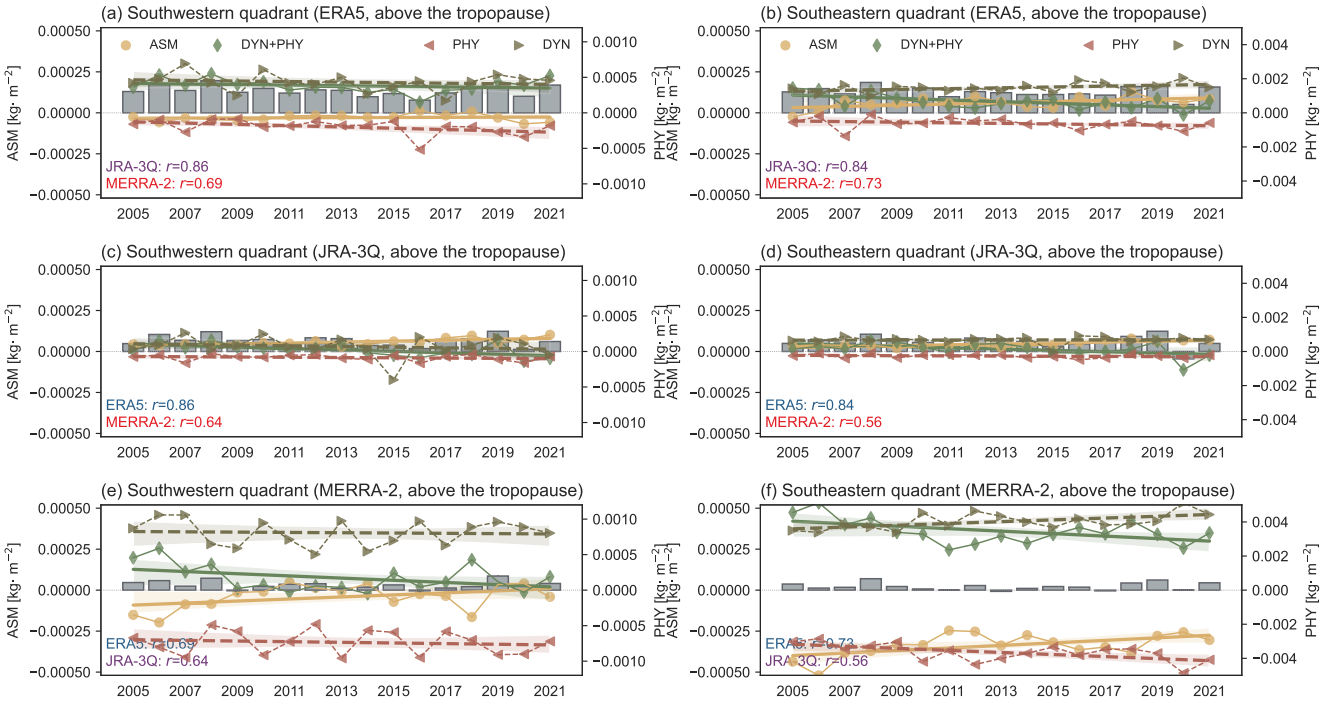

Figure S11. Yearly variations in the sum of the dynamics and physics terms (green lines), assimilation increments (yellow lines), dynamics terms (brown lines), physics increments (red lines), and time rate of changes in partial column water vapor (gray boxes) above the monsoon tropopause layer (68-83 hPa) based on (a,b) ERA5, (c,d) JRA-3Q, and (e,f) MERRA-2 over (a,c,e) the southwestern quadrant (15°N–30°N, 30°E–80°E) and (b,d,f) the southeastern quadrant (15°N–30°N, 80°E–130°E) of the monsoon anticyclone. Correlation coefficients between net water vapor tendency time series based on individual reanalyses are listed in the lower left corner of each panel.

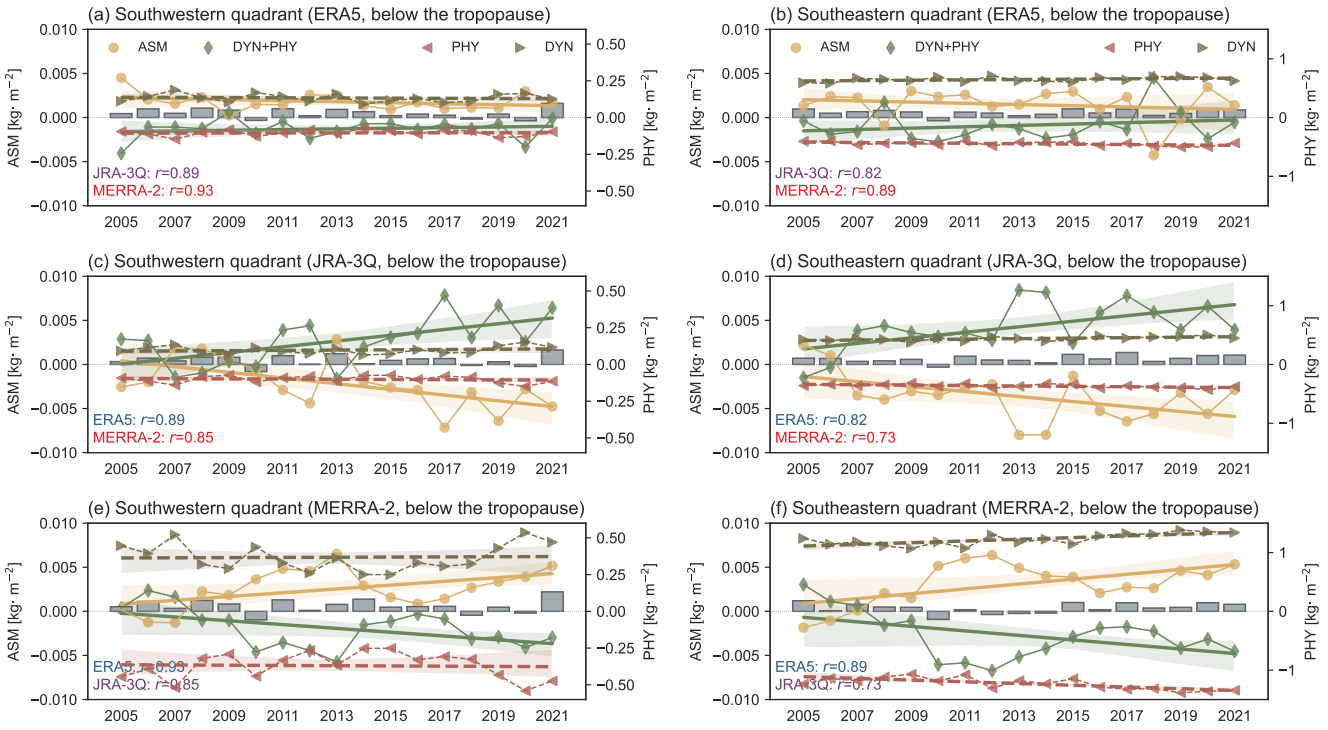

Figure S12. Yearly variations in the sum of the dynamics and physics terms (green lines), assimilation increments (yellow lines), dynamics terms (brown lines), physics increments (red lines), and time rate of changes in partial column water vapor (gray boxes) below the monsoon tropopause layer (100–147 hPa) based on (a,b) ERA5, (c,d) JRA-3Q, and (e,f) MERRA-2 over (a,c,e) the southwestern quadrant (15°N–30°N, 30°E–80°E) and (b,d,f) the southeastern quadrant (15°N–30°N, 80°E–130°E) of the monsoon anticyclone. Correlation coefficients between net water vapor tendency time series based on individual reanalyses are listed in the lower left corner of each panel.

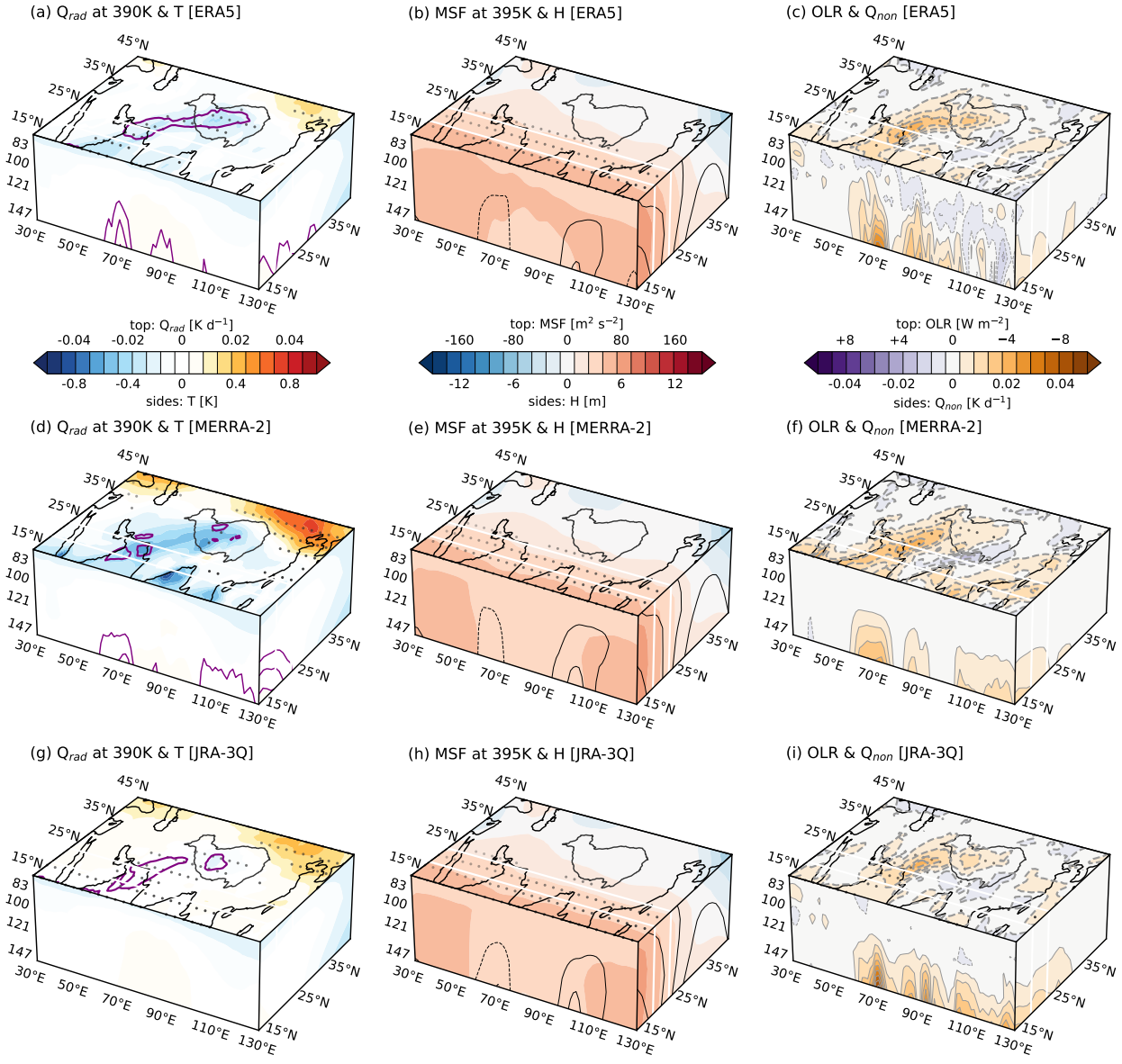

Figure S13. Deseasonalized anomalies regressed onto the interannual variability component of PC1 from Aura MLS in the monsoon tropopause layer (Fig. 3c): (a) radiative heating on the 390 K isentropic surface (shading) and high cloud cover (green contours; top face), and temperature (shading) and cloud ice water content (purple contours; side faces) based on ERA5; (b) Montgomery streamfunction on the 395 K isentropic surface (top face) and geopotential height (shading; side faces) based on ERA5; (c) outgoing longwave radiation (top face; sign reversed) and non-radiative heating (side faces) based on ERA5. (d,e,f) As in (a,b,c) but for MERRA-2. (g,h,i) As in (a,b,c) but for JRA-3Q. Black contours in (b,e,h) indicate anomalies in the meridional (south face) and zonal (east face) wind. The location of the Tibetan Plateau is marked by a dark grey contour and the boundaries of the east–west transect are marked by white lines in all panels. Stippling on the top face indicates locations where regressions are significant at the 95% confidence level.

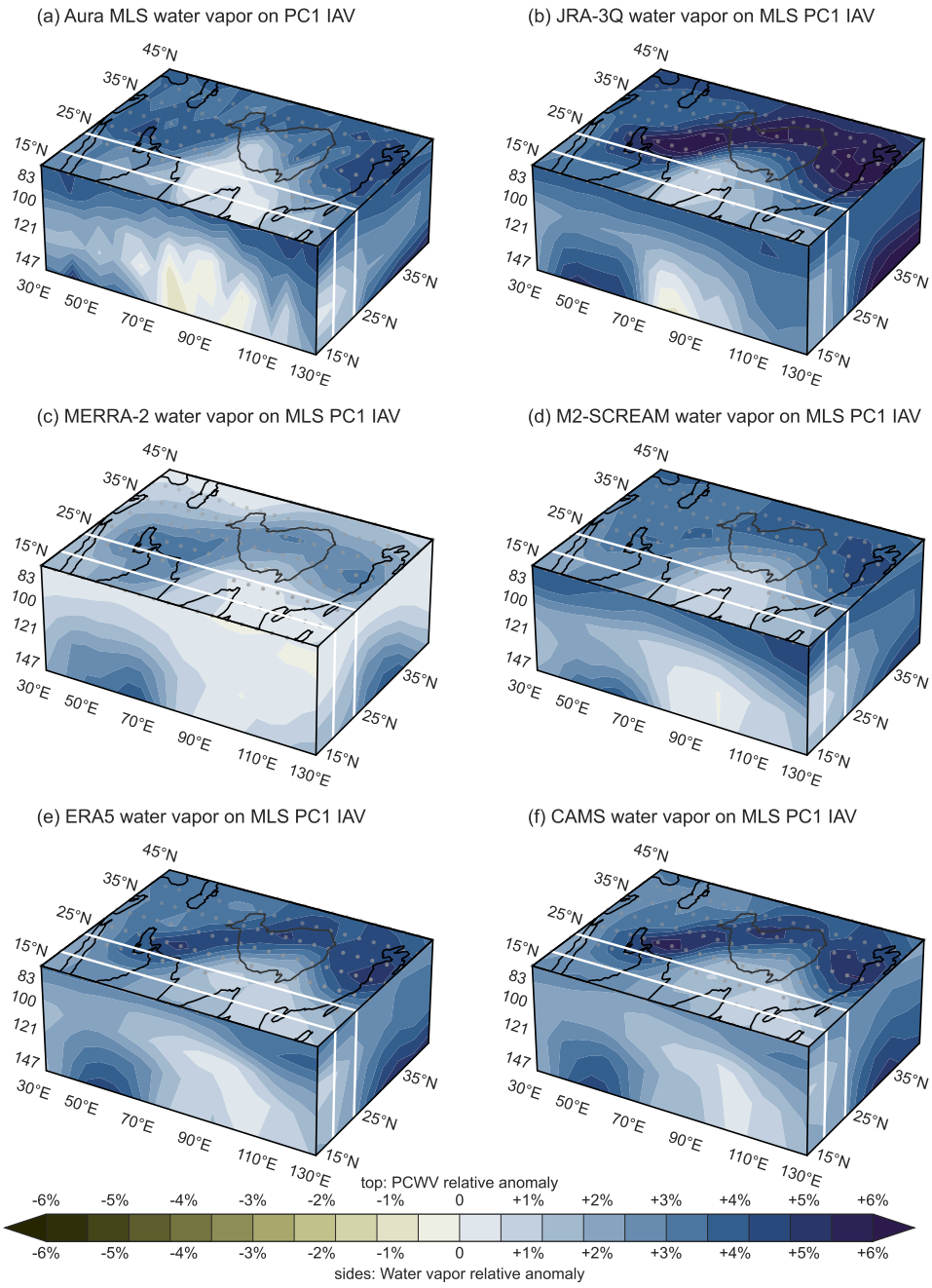

Figure S14. Vertical and horizontal structure of fractional changes in deseasonalized water vapor anomalies regressed onto the interannual variability component of PC1 from Aura MLS (Fig. 3c) based on (a) Aura MLS, (b) JRA-3Q, (c) MERRA-2, (d) M2-SCREAM, (e) ERA5, and (f) CAMS. Fractional anomalies in PCWV are shown on the top face, meridional mean water vapor within 20–25°N along the south face, and zonal mean water vapor within 30–130°E along the east face. The location of the Tibetan Plateau is marked by a dark grey contour and the boundaries of the east–west transect are marked by white lines in all panels. Stippling indicates where PCWV regressions are significant at the 95% confidence level. The figure corresponds to Figure 10c in the main text.

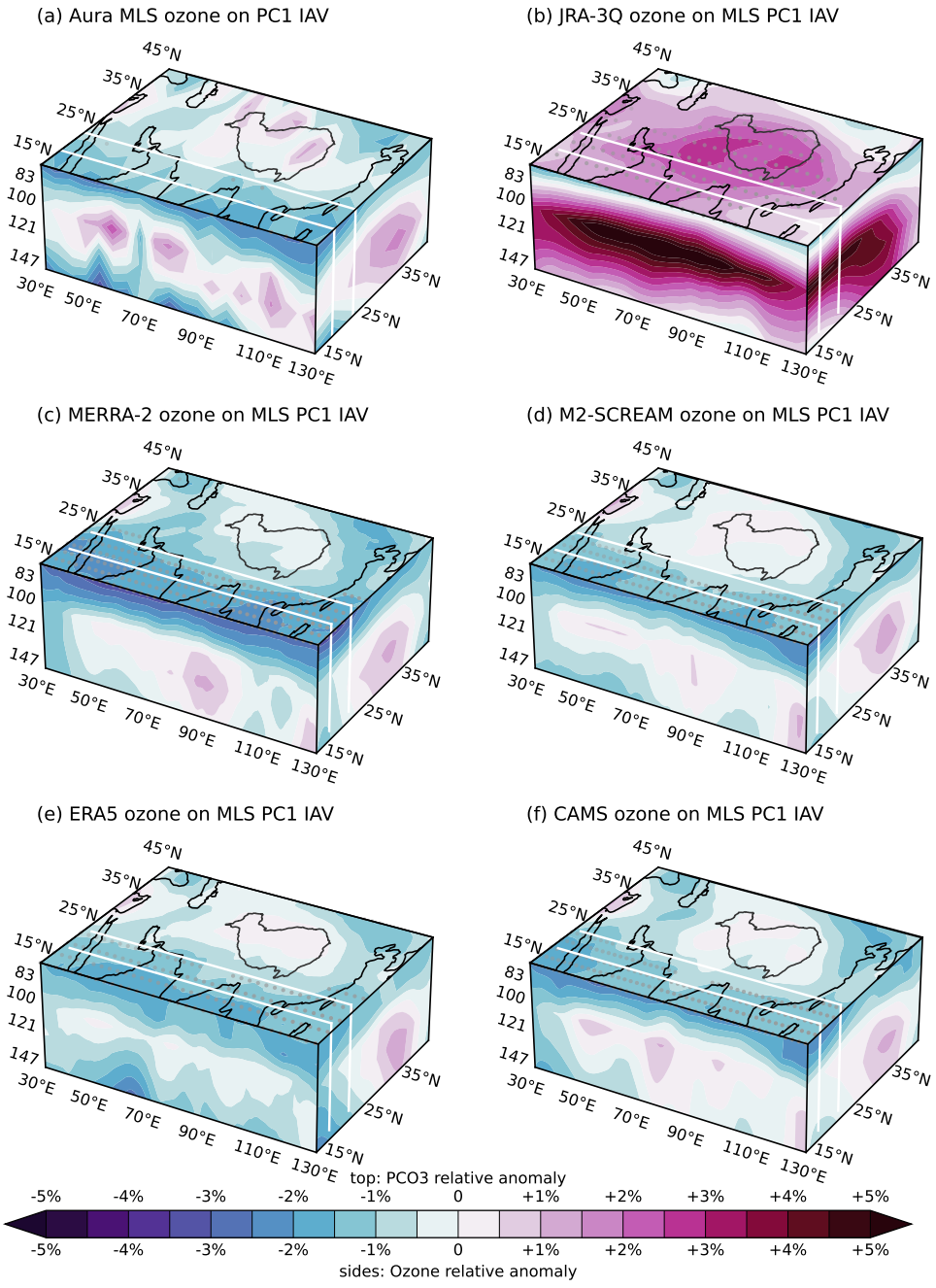

Figure S15. Vertical and horizontal structure of fractional changes in deseasonalized ozone anomalies regressed onto the interannual variability component of PC1 from Aura MLS (Fig. 3c) based on (a) Aura MLS, (b) JRA-3Q, (c) MERRA-2, (d) M2-SCREAM, (e) ERA5, and (f) CAMS. Fractional anomalies in PCO3 are shown on the top face, meridional mean ozone within 20–25°N along the south face, and zonal mean ozone within 30–130°E along the east face. The location of the Tibetan Plateau is marked by a dark grey contour and the boundaries of the east–west transect are marked by white lines in all panels. Stippling indicates where PCO3 regressions are significant at the 95% confidence level.

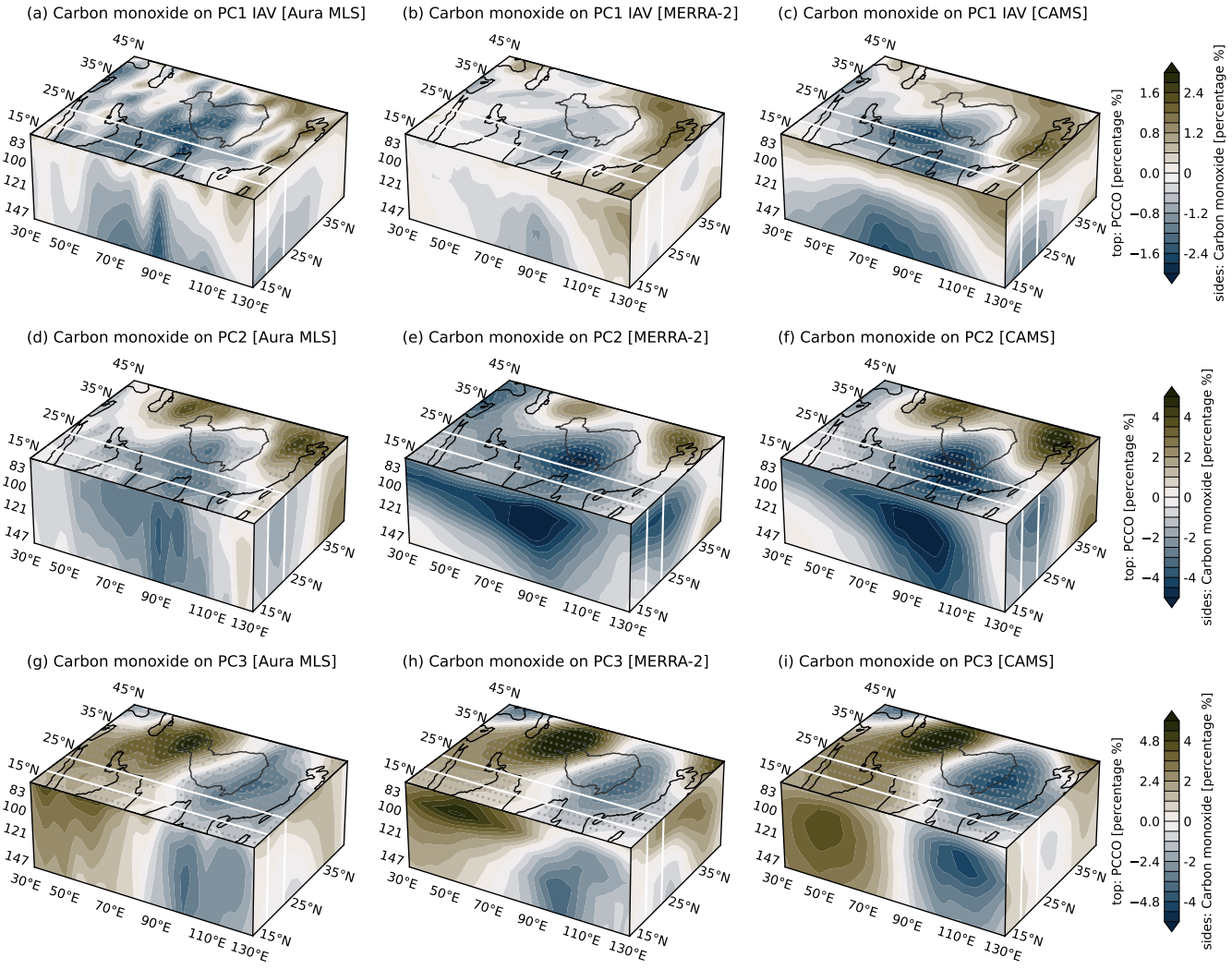

Figure S16. Vertical and horizontal structure of fractional changes in deseasonalized carbon monoxide (CO) anomalies regressed onto the interannual variability component of PC1 from Aura MLS (Fig. 3c) based on (a) Aura MLS, (b) MERRA-2, and (c) CAMS; PC2 of water vapor variability from Aura MLS (Fig. 3d) based on (d) Aura MLS, (e) MERRA-2, and (f) CAMS; and PC3 of water vapor variability from Aura MLS (Fig. 3e) based on (g) Aura MLS, (h) MERRA-2, and (i) CAMS. Fractional anomalies in PCCO are shown on the top faces, meridional mean ozone within 20–25°N along the south faces, and zonal mean ozone within 30–130°E along the east faces. The location of the Tibetan Plateau is marked by a dark grey contour and the boundaries of the east–west transect are marked by white lines in all panels. Stippling indicates where PCCO regressions are significant at the 95% confidence level. The figure corresponds to Figures 10d, 13d, and 14d in the main text.

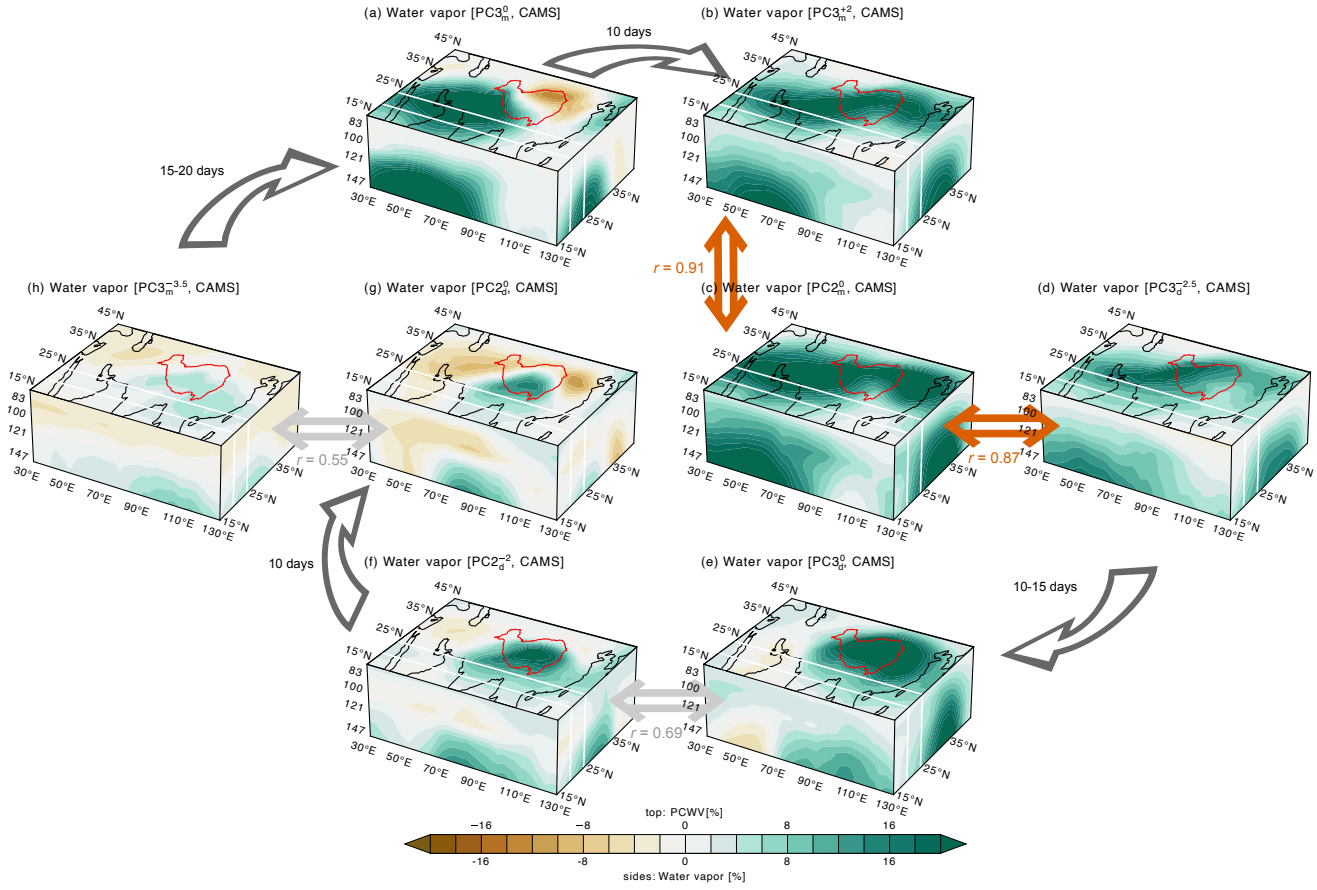

Figure S17. Distributions of tropopause layer water vapor anomalies illustrating the quadratic cycle of water vapor sub-seasonal variability based on CAMS. Water vapor relative anomalies are composited for the (a) principal component (PC3) moist phase, (b) two pentads after the PC3 moist phase, (c) the PC2 moist phase, (d) 2.5 pentads before the PC3 dry phase, (e) the PC3 dry phase, (f) two pentads before the PC2 dry phase, (g) the PC2 dry phase, and (h) 3.5 pentads before the PC3 moist phase. Area-weighted pattern correlations in PCWV between matched distributions are noted next to each set of double arrows. Curved arrows indicate transitions. The location of the Tibetan Plateau is marked by a red contour and the boundaries of the east–west transect are marked by white lines in all panels.

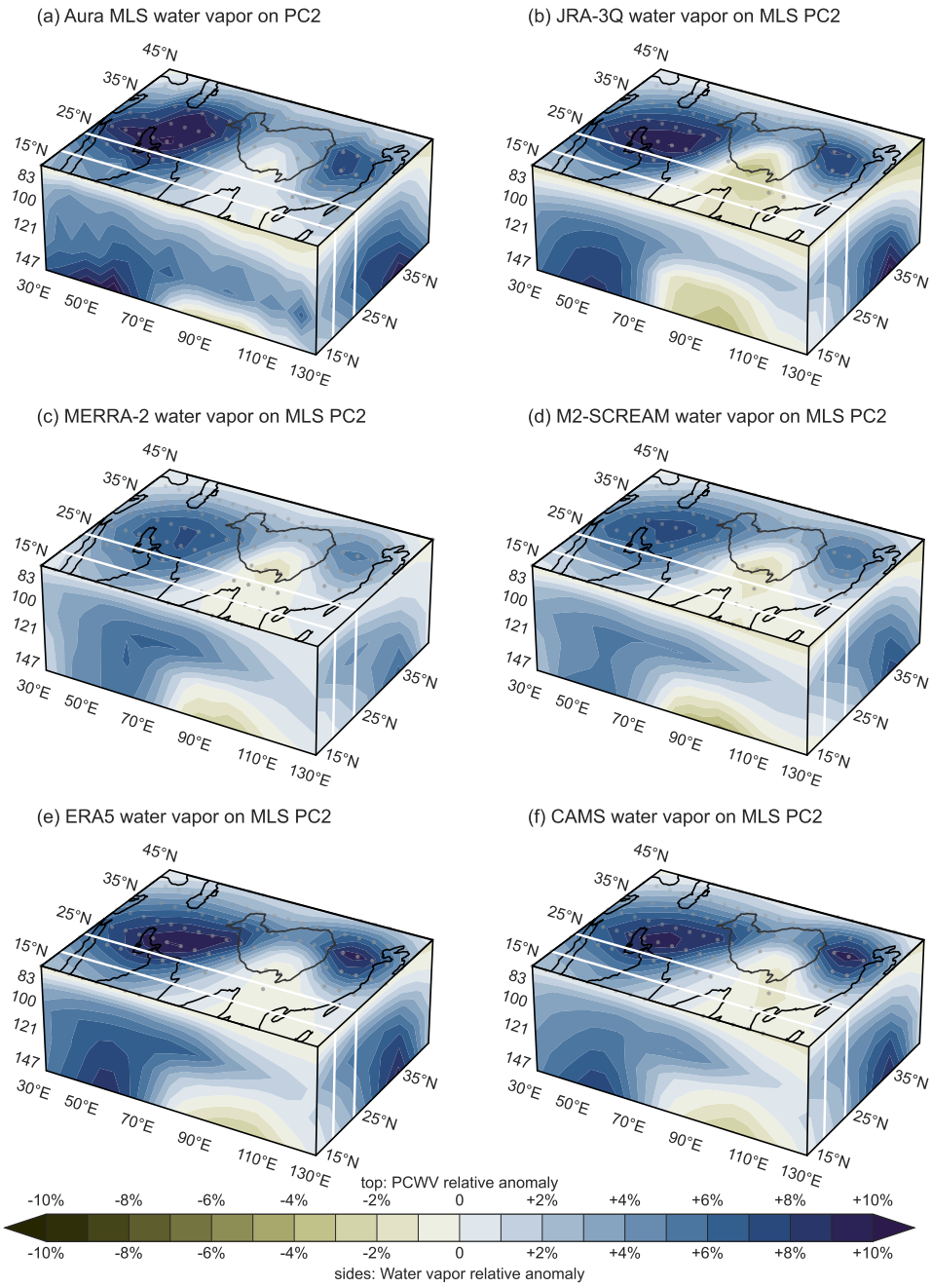

Figure S18. Vertical and horizontal structure of fractional changes in deseasonalized water vapor anomalies regressed onto PC2 from Aura MLS (Fig. 3d) based on (a) Aura MLS, (b) JRA-3Q, (c) MERRA-2, (d) M2-SCREAM, (e) ERA5, and (f) CAMS. Fractional anomalies in PCWV are shown on the top face, meridional mean water vapor within 20–25°N along the south face, and zonal mean water vapor within 30–130°E along the east face. The location of the Tibetan Plateau is marked by a dark grey contour and the boundaries of the east–west transect are marked by white lines in all panels. Stippling indicates where PCWV regressions are significant at the 95% confidence level. The figure corresponds to Figure 12b in the main text.

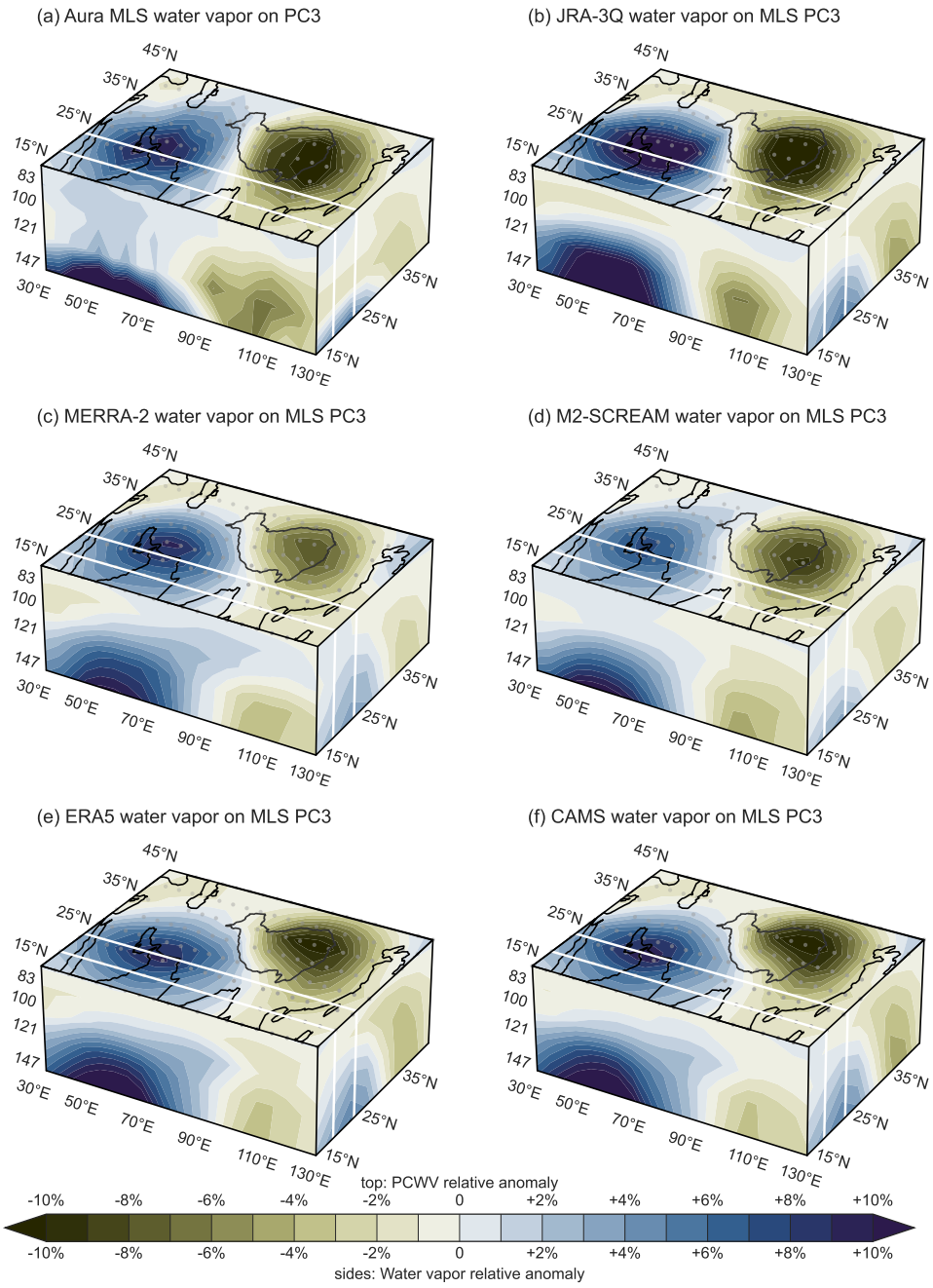

Figure S19. Vertical and horizontal structure of fractional changes in deseasonalized water vapor anomalies regressed onto PC3 from Aura MLS (Fig. 3e) based on (a) Aura MLS, (b) JRA-3Q, (c) MERRA-2, (d) M2-SCREAM, (e) ERA5, and (f) CAMS. Fractional anomalies in PCWV are shown on the top face, meridional mean water vapor within 20–25°N along the south face, and zonal mean water vapor within 30–130°E along the east face. The location of the Tibetan Plateau is marked by a dark grey contour and the boundaries of the east–west transect are marked by white lines in all panels. Stippling indicates where PCWV regressions are significant at the 95% confidence level. The figure corresponds to Figure 12a in the main text.

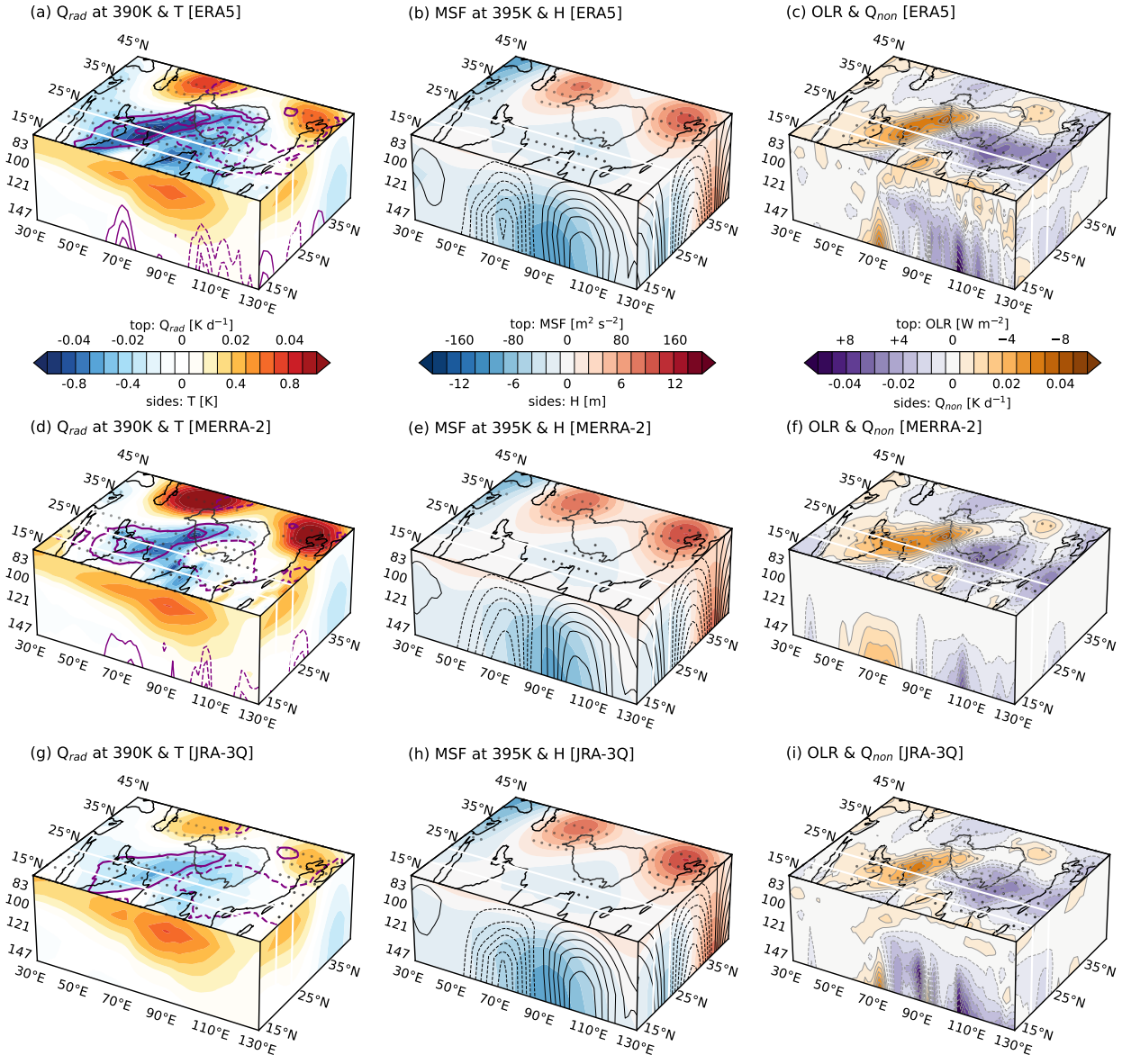

Figure S20. Deseasonalized anomalies regressed onto the second principal component (PC2) of water vapor variability in the monsoon tropopause layer based on Aura MLS (Fig. 3d): (a) radiative heating on the 390 K isentropic surface (shading) and high cloud cover (purple contours; top face), and temperature (shading) and cloud ice water content (purple contours; side faces) based on ERA5; (b) Montgomery streamfunction on the 395 K isentropic surface (top face) and geopotential height (shading; side faces) based on ERA5; (c) outgoing longwave radiation (top face; sign reversed) and non-radiative heating (side faces) based on ERA5. (d,e,f) As in (a,b,c) but for MERRA-2. (g,h,i) As in (a,b,c) but for JRA-3Q. Black contours in (b,e,h) indicate anomalies in the meridional (south face) and zonal (east face) wind. The location of the Tibetan Plateau is marked by a dark grey contour and the boundaries of the east–west transect are marked by white lines in all panels. Stippling on the top face indicates locations where regressions are significant at the 95% confidence level.

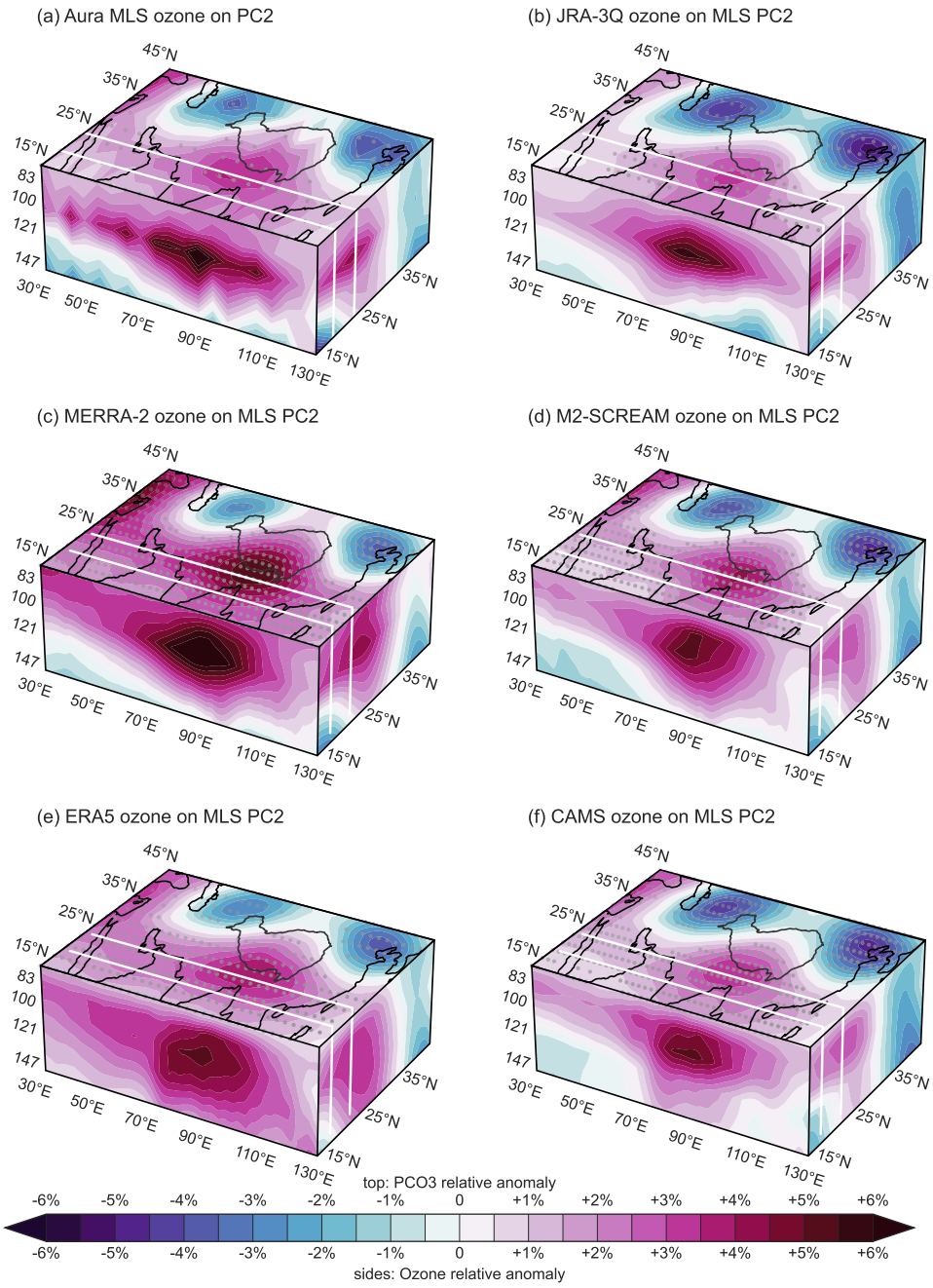

Figure S21. Vertical and horizontal structure of fractional changes in deseasonalized ozone anomalies regressed onto PC2 from Aura MLS (Fig. 3d) based on (a) Aura MLS, (b) JRA-3Q, (c) MERRA-2, (d) M2-SCREAM, (e) ERA5, and (f) CAMS. Fractional anomalies in PCO3 are shown on the top face, meridional mean ozone within 20–25°N along the south face, and zonal mean ozone within 30–130°E along the east face. The location of the Tibetan Plateau is marked by a dark grey contour and the boundaries of the east–west transect are marked by white lines in all panels. Stippling indicates where PCO3 regressions are significant at the 95% confidence level. The figure corresponds to Figure 14c in the main text.

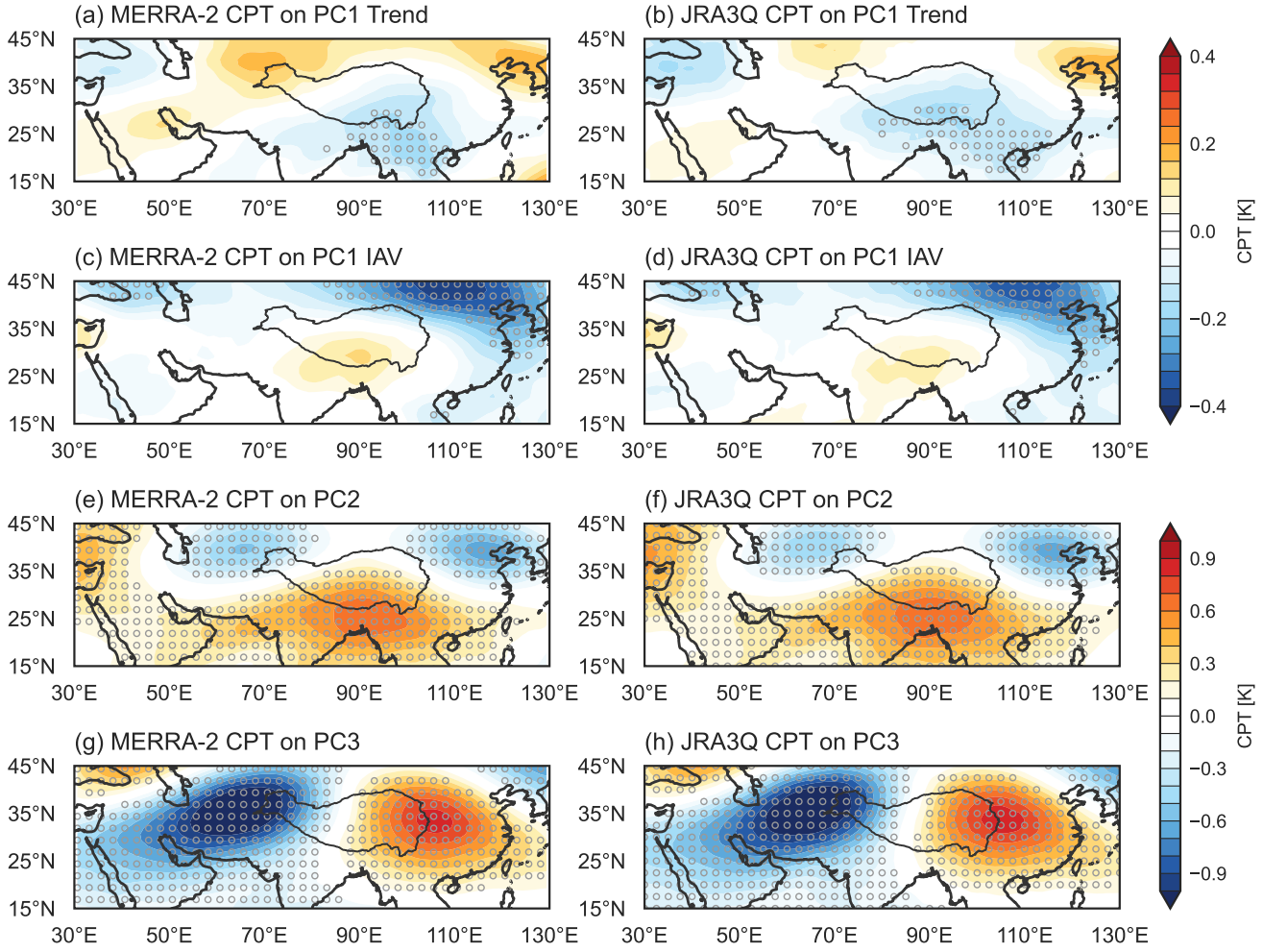

Figure S22. Deseasonalized anomalies of cold point tropopause (CPT) temperatures based on (a,c,e,g) MERRA-2 and (b,d,f,h) JRA-3Q regressed into (a)–(b) the PC1 trend component (Fig. 3b), (c)–(d) the PC1 interannual variability component (Fig. 3c), (e)–(f) PC2 (Fig. 3d), and (g)–(h) PC3 (Fig. 3e) from Aura MLS (see main text for details). The location of the Tibetan Plateau is marked by a dark grey contour in all panels. Stippling indicates that regressions are significant at the 95% confidence level. The figure corresponds to distributions of cold point temperature anomalies in Figures 6,15 of the main text.

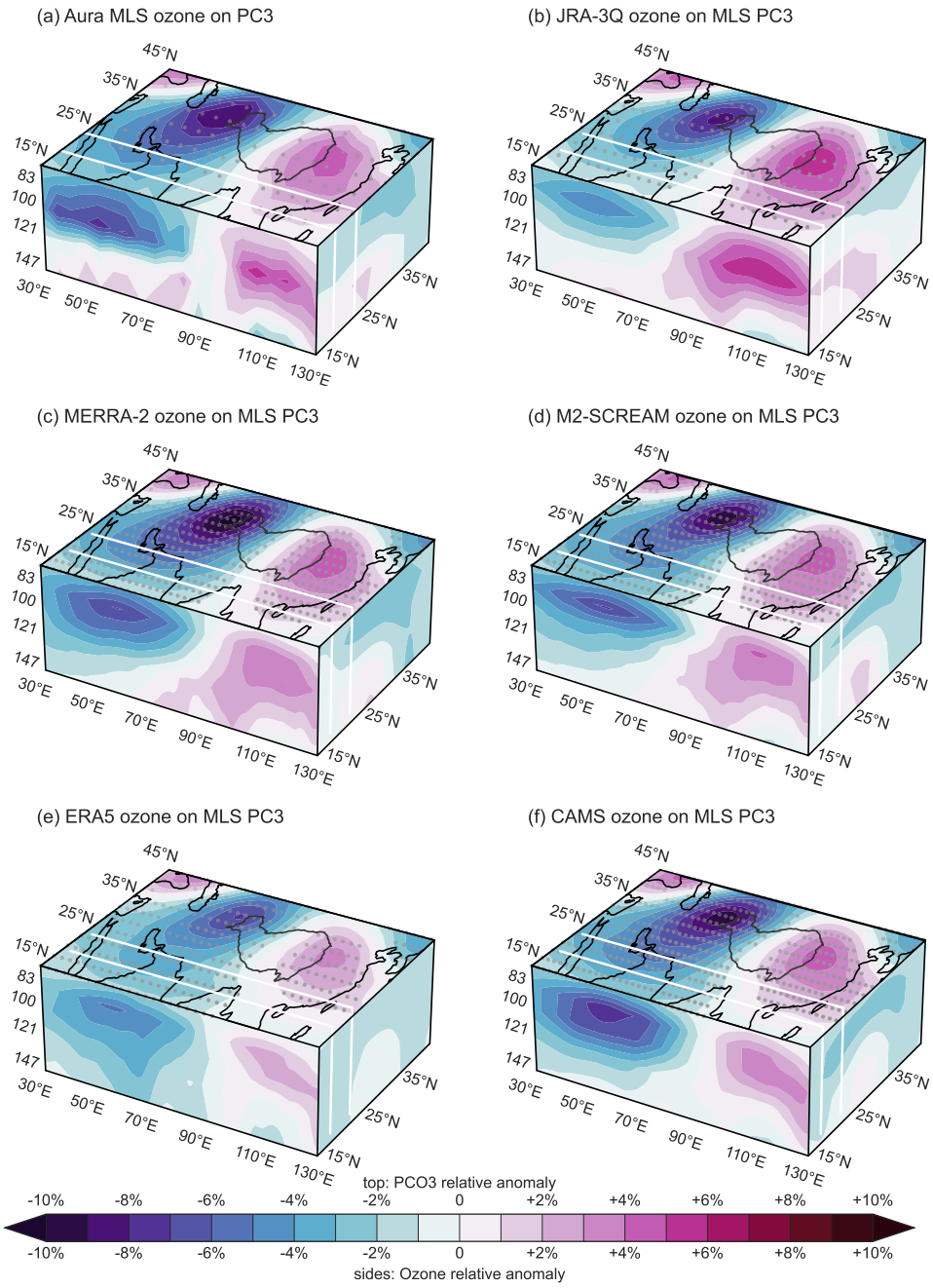

Figure S23. Vertical and horizontal structure of fractional changes in deseasonalized ozone anomalies regressed onto PC3 from Aura MLS (Fig. 3e) based on (a) Aura MLS, (b) JRA-3Q, (c) MERRA-2, (d) M2-SCREAM, (e) ERA5, and (f) CAMS. Fractional anomalies in PCO3 are shown on the top face, meridional mean ozone within 20–25°N along the south face, and zonal mean ozone within 30–130°E along the east face. Dark grey contours mark the location of the Tibetan Plateau and white lines mark the boundaries of the east–west transect in all panels. Stippling indicates where PCO3 regressions are significant at the 95% confidence level. The figure corresponds to Figure 13c in the main text.

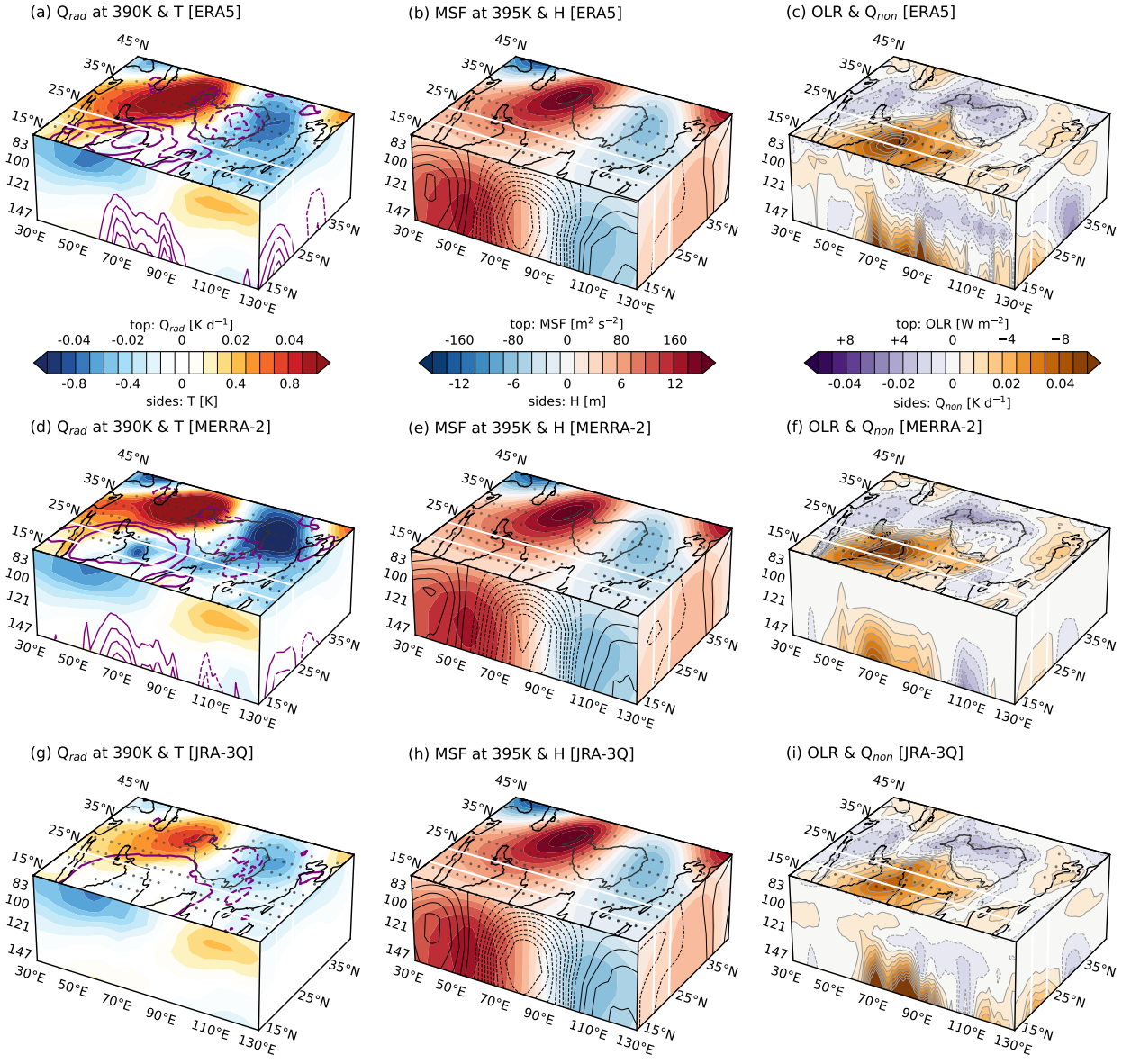

Figure S24. Deseasonalized anomalies regressed onto the third principal component (PC3) of water vapor variability in the monsoon tropopause layer based on Aura MLS (Fig. 3e): (a) radiative heating on the 390 K isentropic surface (shading) and high cloud cover (purple contours; top face), and temperature (shading) and cloud ice water content (purple contours; side faces) based on ERA5; (b) Montgomery streamfunction on the 395 K isentropic surface (top face) and geopotential height (shading; side faces) based on ERA5; (c) outgoing longwave radiation (top face; sign reversed) and non-radiative heating (side faces) based on ERA5. (d,e,f) As in (a,b,c) but for MERRA-2. (g,h,i) As in (a,b,c) but for JRA-3Q. Black contours in (b,e,h) indicate anomalies in the meridional (south face) and zonal (east face) wind. The location of the Tibetan Plateau is marked by a dark grey contour and the boundaries of the east–west transect are marked by white lines in all panels. Stippling on the top face indicates locations where regressions are significant at the 95% confidence level.

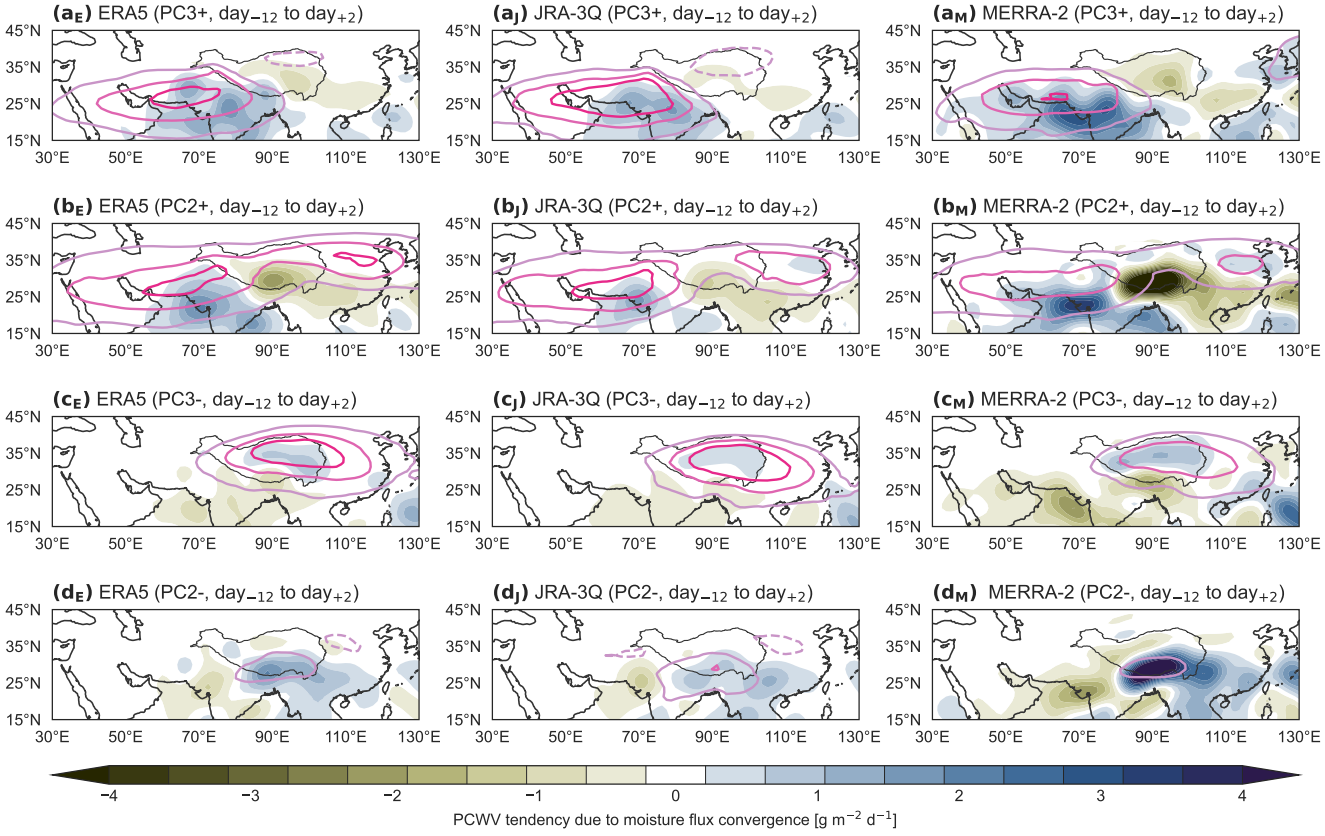

Figure S25. Anomalous water vapor tendencies due to dynamics (i.e. moisture flux convergence) for (a_E–d_E) ERA5, (a_J–d_J) JRA-3Q, and (a_M–d_M) MERRA-2 during the 15 days ending on episodes of (a) positive PC3 > 1 (PC3+), (b) positive PC2 > 1 (PC2+), (c) negative PC3 < −1 (PC3−), and (d) negative PC2 < −1 (PC2−). Anomalies in partial column water vapor are marked with pink contours at intervals of 10% from ±10% (negative dashed) during each phase. The location of the Tibetan Plateau is marked by a dark grey contour in all panels.

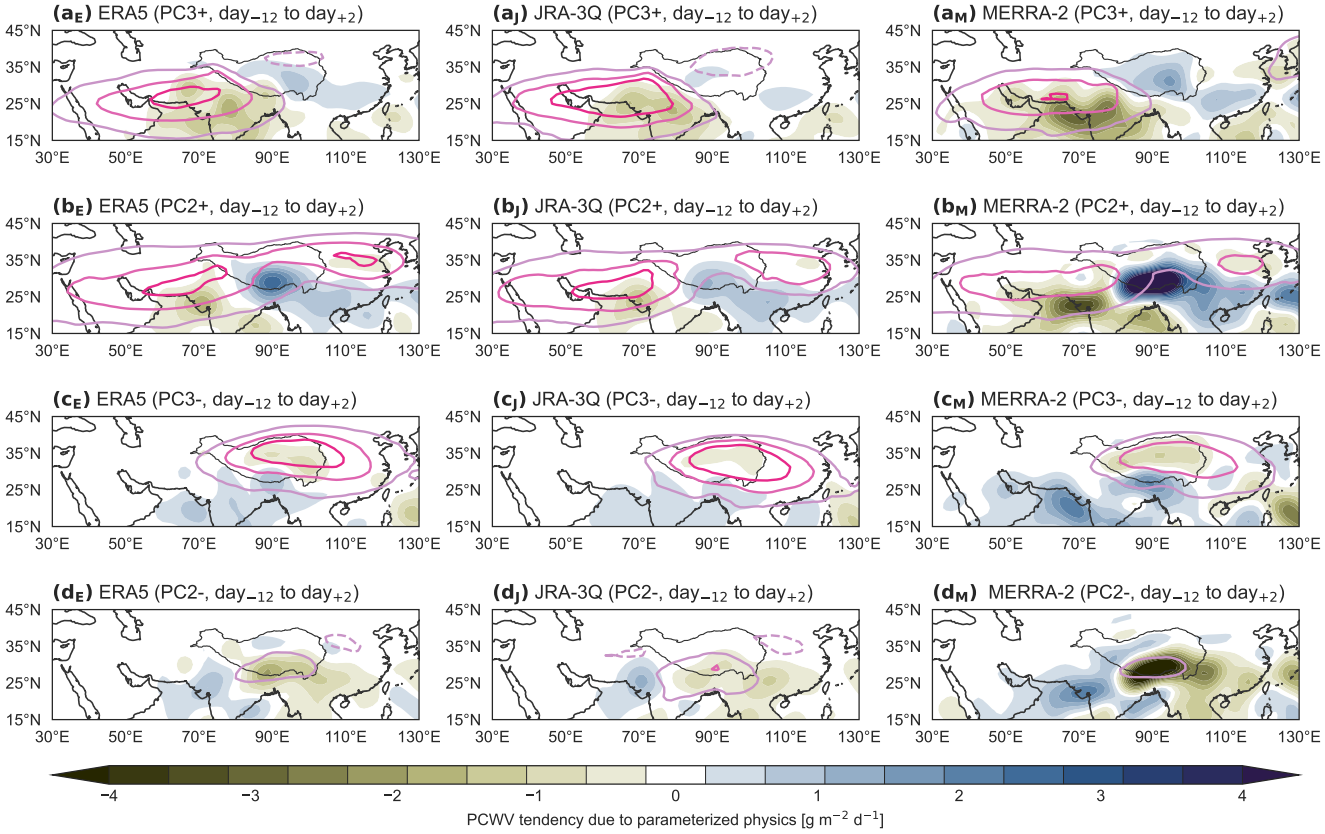

Figure S26. Anomalous water vapor tendencies due to parameterized physics for (a_E–d_E) ERA5, (a_J–d_J) JRA-3Q, and (a_M–d_M) MERRA-2 during the 15 days ending on episodes of (a) positive PC3 > 1 (PC3+), (b) positive PC2 > 1 (PC2+), (c) negative PC3 < −1 (PC3−), and (d) negative PC2 < −1 (PC2−). Anomalies in partial column water vapor are marked with pink contours at intervals of 10% from ±10% (negative dashed) during each phase. The location of the Tibetan Plateau is marked by a dark grey contour in all panels.

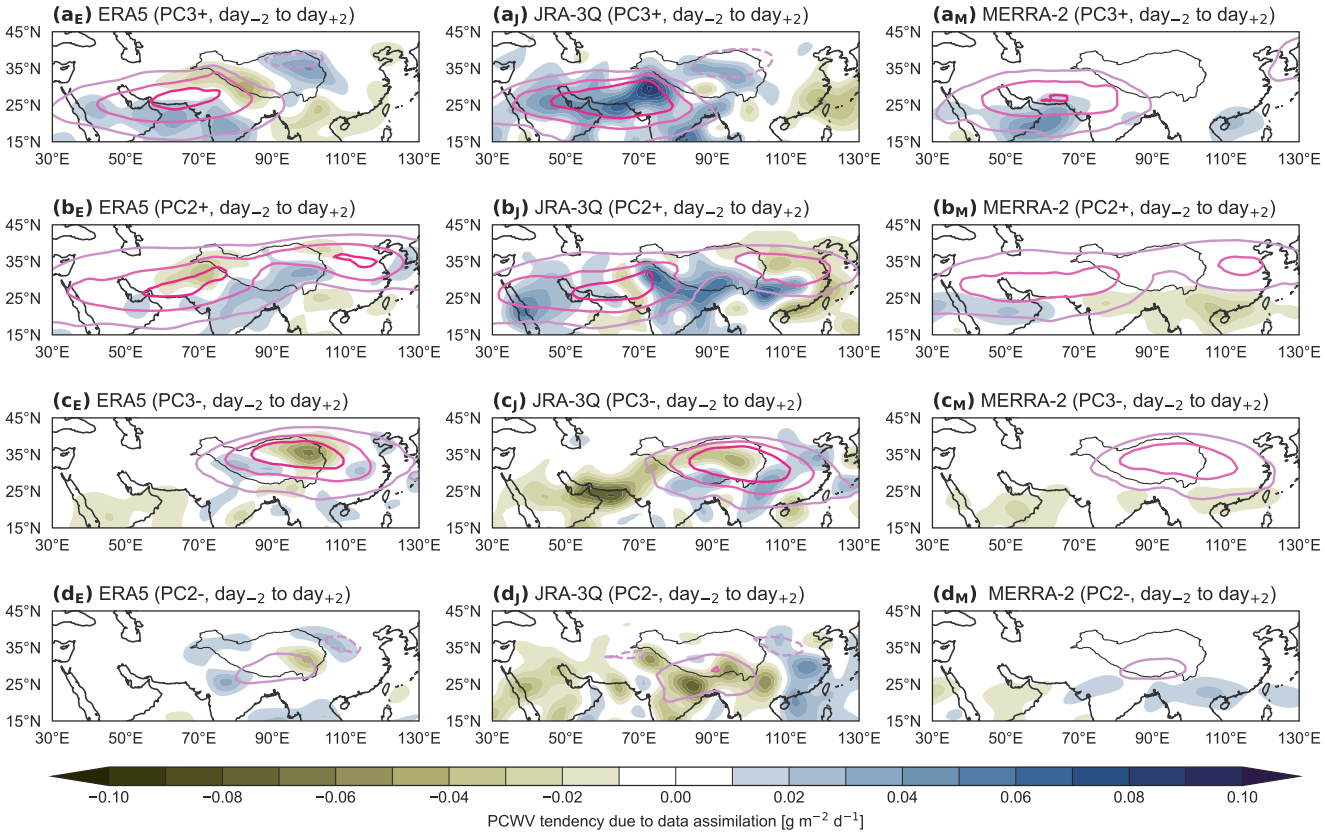

Figure S27. Anomalous water vapor tendencies due to data assimilation for (a_E–d_E) ERA5, (a_J–d_J) JRA-3Q, and (a_M–d_M) MERRA-2 during the 15 days ending on episodes of (a) positive PC3 > 1 (PC3+), (b) positive PC2 > 1 (PC2+), (c) negative PC3 < −1 (PC3−), and (d) negative PC2 < −1 (PC2−). Anomalies in partial column water vapor are marked with pink contours at intervals of 10% from ±10% (negative dashed) during each phase. The location of the Tibetan Plateau is marked by a dark grey contour in all panels. The MERRA-2 assimilation term includes the stratospheric nudging tendency.